

# DFT2kp: effective $\mathbf{k} \cdot \mathbf{p}$ models from *ab-initio* data

João Victor V. Cassiano,<sup>1,2</sup> Augusto L. Araújo,<sup>1,3</sup> Paulo E. Faria Junior,<sup>4</sup> and Gerson J. Ferreira<sup>1</sup>

<sup>1</sup>*Instituto de Física, Universidade Federal de Uberlândia, Uberlândia, MG 38400-902, Brazil*

<sup>2</sup>*Instituto de Física, Universidade de São Paulo, São Paulo, SP, 05508-090, Brazil*

<sup>3</sup>*Ilum School of Science, CNPEM, C.P. 6192, 13083-970, Campinas, SP, Brazil*

<sup>4</sup>*Institute for Theoretical Physics, University of Regensburg, 93040 Regensburg, Germany*

The  $\mathbf{k} \cdot \mathbf{p}$  method and group theory provide straightforward analytical expressions for the low energy effective Hamiltonians of crystalline materials, however it does not provide the numerical values for its coefficients. These are typically cast as matrix elements of the generalized momentum operator  $\boldsymbol{\pi} = \mathbf{p} + \mathbf{p}_{\text{SOC}}$ , which includes spin-orbit coupling corrections. Their numerical values are usually obtained by fitting either experimental data, or fitting the *ab initio* band structure. Here we develop a code to explicitly calculate the Kane and Luttinger parameters of  $\mathbf{k} \cdot \mathbf{p}$  effective Hamiltonians directly from *ab initio* wave-functions provided by Quantum Espresso. Additionally, the code analyzes the symmetry transformations of the wave-functions to optimize the final Hamiltonian. This an optional step in the code, where it numerically finds the unitary transformation  $U$  that rotates the basis towards an optimal representation informed by the user. Throughout the paper we present the methodology in detail, and illustrate the capabilities of the code applying it to a selection of relevant materials. Particularly, we show a “hands on” example on how to run the code for graphene. The code is open source and available at <https://gitlab.com/dft2kp/dft2kp>.

## I. INTRODUCTION

The band structure of crystalline materials define most of its electronic properties, and its accurate description is essential to the development of novel devices. For this reason, the *ab initio* density functional theory (DFT) [1, 2] provides one of the most successful tools for the development of electronics, spintronics, optoelectronics, etc. The DFT methods have been implemented in a series of codes (*e.g.*, Quantum Espresso [3, 4], VASP [5], Wien2K [6], Gaussian [7], DFTB+ [8], Siesta [9, 10], ...), which differ by the choice of basis functions (*e.g.*, localized orbitals or plane-waves), pseudo-potential approximations, and other functionalities. Nevertheless, all DFT implementations provide methods to obtain the equilibrium (relaxed) crystalline structure, phonon dispersion, and electronic band structures. Complementary, few bands effective models are essential to further study transport, optical, and magnetic properties of crystalline materials. These can be developed either via the tight-binding (TB) [11–13] or  $\mathbf{k} \cdot \mathbf{p}$  method [14, 15], which complement each other.

On the one hand, the TB method has an “atomistic” nature, since it is built upon localized basis sets (*e.g.*, maximally-localized Wannier functions [16], or atomic orbitals), which makes this method optimal for numerical modeling of transport, optical and other properties of complex *nanomaterials* [17–20].

On the other hand, the  $\mathbf{k} \cdot \mathbf{p}$  method uses basis sets of extended waves, which are exact solutions of the Hamiltonian at the relevant quasi-momentum, typically at a high symmetry point of the Brillouin zone. While this characteristic may limit the  $\mathbf{k} \cdot \mathbf{p}$  description to a narrow region of the energy-momentum space, the  $\mathbf{k} \cdot \mathbf{p}$  Hamiltonians are easier to handle analytically and, specially, are very suitable to study mesoscopic systems using the envelope function approximation [21–26]. For example, the  $\mathbf{k} \cdot \mathbf{p}$

framework has been successfully applied to study nanostructures (quantum wells, wires, and dots) [27–29], topological insulators [30–32], spin-lasers [33, 34], polytypism [35–37], as well as a large variety of two-dimensional van der Waals materials [38–41]. Moreover, recent developments in the field of transition metal dichalcogenides (TMDCs) have combined DFT and  $\mathbf{k} \cdot \mathbf{p}$  methodologies to explore the valley Zeeman physics in TMDC monolayers and their van der Waals heterostructures [42–45].

Both the TB and  $\mathbf{k} \cdot \mathbf{p}$  Hamiltonians are defined in terms of arbitrary coefficients. In the TB case, these are local site energies and hopping amplitudes described by Slater-Koster matrix elements [11]. For the  $\mathbf{k} \cdot \mathbf{p}$  Hamiltonians, these are the Kane [46, 47] and Luttinger [48] parameters, which are matrix elements of the momentum and spin-orbit coupling operators. In all cases, the coefficients are typically obtained either (i) comparing the theoretical predictions (band structure, transport, or optical properties) to available experimental data [15, 49], or (ii) fitting to the DFT data [39, 41, 50–53]. For instance, the `wannier90` code [54, 55] obtains optimal TB models by fitting the DFT data. Additionally, TB models can be numerically obtained directly from the DFT atomic orbitals by the explicitly calculation of the Slater-Koster matrix elements (*e.g.*, see the `paoflow` [56], and DFTB+ [8] codes). In contrast, while it is possible to extract  $\mathbf{k} \cdot \mathbf{p}$  models from a Taylor expansion on top of a TB model (*e.g.*, via the code `tbmodels` [57]), there are no available codes to calculate the  $\mathbf{k} \cdot \mathbf{p}$  Kane and Luttinger parameters directly from the DFT wave-functions.

To calculate the  $\mathbf{k} \cdot \mathbf{p}$  matrix elements from the DFT wave-functions, one needs to account for how the wave-function are represented in the DFT code [58, 59]. For instance, Quantum Espresso and VASP implement pseudopotential approximations within the Projector Augmented Wave (PAW) method [60–63]. Fortunately, Quantum Espresso already provides a routine to calcu-

late matrix elements of the velocity operator (which is sufficient to obtain  $\mathbf{k} \cdot \mathbf{p}$  models, as we see in Section B). Indeed, recently, Jocić and collaborators [64] have successfully calculated  $\mathbf{k} \cdot \mathbf{p}$  models directly from QE’s wave-functions (see disclaimer at our Conclusions).

In this paper, we present an *open-source code* that automatically calculates the numerical values for the  $\mathbf{k} \cdot \mathbf{p}$  Kane and Luttinger parameters using the wave-functions provided by Quantum Espresso (QE). For this purpose, first, we develop a patch to instruct QE to calculate and store the matrix elements of the generalized momentum  $\boldsymbol{\pi} = \mathbf{p} + \mathbf{p}_{\text{SOC}}$ , which includes the spin-orbit corrections. Together with the eigenenergies  $E_n^0$  at  $\mathbf{k}_0$ , the matrix elements of  $\boldsymbol{\pi}$  for a selected set of  $N$  bands define the effective  $\mathbf{k} \cdot \mathbf{p}$  Hamiltonian  $H_{N \times N}(\mathbf{k})$  for  $\mathbf{k}$  near  $\mathbf{k}_0$ . Our python package reads these matrix elements and QE’s wave-functions  $|n\rangle$  to automatically build  $H_{N \times N}(\mathbf{k})$  using Löwdin’s partitioning for the folding down of all QE bands into the selected  $N$  bands subspace. Additionally, the user has the option to improve the *appearance* (or *shape*) of the effective Hamiltonian via a symmetry optimization process aided by the `qsymm` package [65], which builds the symbolic Hamiltonian via group theory and the method of invariants. To illustrate the capabilities of our code, we show here a step-by-step “hands-on” tutorial on how to run the code for graphene, and later we present results for selected materials [zincblende, wurtzite, rock-salt, transition metal dichalcogenides (TMDC), and others]. In all cases, the modeled band structure matches remarkably well the DFT data at low energies near the expansion point  $\mathbf{k}_0$ . Our code is open source and available at the `gitlab` repository [66].

This paper is organized as follows. In Section II we present our methodology starting with a brief review of the  $\mathbf{k} \cdot \mathbf{p}$  method, Löwdin partitioning, the method of invariants, the symmetry optimization process, and the calculation of matrix elements using the DFT data. Next, in Section III, we show the code in detail using graphene as a practical example. Later, in Section IV, we illustrate the results of the code for zincblend (GaAs, CdTe, HgTe), wurtzite (GaP, GaN, InP), rock-salt (SnTe, PbSe), a TMDC (MoS<sub>2</sub>), and other materials (Bi<sub>2</sub>Se<sub>3</sub>, GaBiCl<sub>2</sub>). We finish the paper with an overview of the results in Section V, and the conclusions.

## II. METHODS

Our goal is to obtain the numerical values for the coefficients of  $\mathbf{k} \cdot \mathbf{p}$  effective Hamiltonians [14, 15]. Namely, these are the Kane [46, 47] and Luttinger [48] parameters. To present our approach for this calculation, let us start by briefly describing its fundamental steps. First, we review the  $\mathbf{k} \cdot \mathbf{p}$  method to show that these coefficients depend only upon matrix elements of the type  $\mathbf{P}_{m,n} = \langle m | \boldsymbol{\pi} | n \rangle$ , where  $\boldsymbol{\pi} = \mathbf{p} + \mathbf{p}_{\text{SOC}}$  is the generalized momentum operator with the spin-orbit corrections, and  $\{|n\rangle\}$  is the set of numerical wave-functions

obtained from the *ab initio* DFT simulations (e.g. via Quantum Espresso [3, 4]). However, the numerical basis given by  $\{|n\rangle\}$  does not match, *a priori*, the optimal basis set that yields the desired *shape* for effective  $\mathbf{k} \cdot \mathbf{p}$  Hamiltonian. Therefore, to properly identify the Kane and Luttinger parameters, we perform a *symmetry optimization*, which rotates the arbitrary numerical basis into the optimal form. This symmetry optimization is performed via group theory [67, 68] by enforcing that the numerical DFT basis transform under the same representation of an *optimal* basis, which is informed by the user.

In summary, the algorithm steps are:

1. Read the QE/DFT data: energies  $E_n^0$  and eigenstates  $|n\rangle$  at the selected  $\mathbf{k}_0$  point.
2. Calculate or read the matrix elements of  $\mathbf{P}_{m,n} = \langle m | \boldsymbol{\pi} | n \rangle$  for all bands  $(m, n)$ .
3. Select the bands of interest (set  $\alpha$ ). The code will identify the irreducible representations of the bands using the `IrRep` python package [69], and present it as a report to the user. Additionally, the code calculates the model folded down into the selected set  $\alpha$  via Löwdin partitioning.
4. Build the optimal effective model from symmetry constraints using the `Qsymm` python package [65] under an optimal basis informed by the user. This optimal basis must be in a set of representations equivalent to the ones identified in step 3.
5. Calculate the representation matrices for the symmetry operators in the original QE basis  $|n\rangle$ . The code verifies if the representations of numerical QE basis are equivalent to the representations of the optimal basis from step 4.
6. Calculates the transformation matrix  $U$  that rotates the original QE basis into the optimal basis set on step 4. Applies the transformation  $U$  and calculates the optimal numerical effective Hamiltonian.
7. Convert values from Rydberg atomic units into meV and nm units, and presents a report with values for the  $\mathbf{k} \cdot \mathbf{p}$  parameters.

In the next sections we describe the relevant details of the steps above, but not following the algorithmic order above. More specifically, in Section II A, we briefly review the  $\mathbf{k} \cdot \mathbf{p}$  formalism to show that  $\mathbf{P}_{m,n} = \langle m | \boldsymbol{\pi} | n \rangle$  plays a central role in our approach. Incidentally, we introduce the folding down via Löwdin partitioning. Next, we define what is the optimal *shape* of the Hamiltonian via method of invariants [15, 70] in Section II B. In Section II C, we present the symmetry optimization approach to calculate the transformation matrix  $U$  that yields our final  $H^{\text{optimal}} = U \cdot H^{\text{DFT}} \cdot U^\dagger$ . At last, in Section II D we discuss how  $\mathbf{P}_{m,n} = \langle m | \boldsymbol{\pi} | n \rangle$  is calculated.

Throughout the paper we use atomic Rydberg units (a.u.), thus the reduced Planck constant, bare electron mass and charge are  $\hbar = 2m_0 = e^2/2 = 1$ , the permittivity of vacuum is  $4\pi\epsilon_0 = 1$ , the speed of light is  $c = 2/\alpha \approx 274$ , and  $\alpha \approx 1/137$  is the fine structure constant.

### A. The $\mathbf{k} \cdot \mathbf{p}$ model

In this section we briefly review the  $\mathbf{k} \cdot \mathbf{p}$  method [14, 15, 46–48] and the folding down via Löwdin partitioning [15, 70] to establish our notation.

We are interested in the effective Hamiltonian near a high symmetry point  $\mathbf{k}_0$  of the Brillouin zone. Therefore, we write the quasi-momentum as  $\boldsymbol{\kappa} = \mathbf{k}_0 + \mathbf{k}$ , such that  $\mathbf{k}$  is the deviation from  $\mathbf{k}_0$ . The Bloch theorem allow us to decompose the wave-function as  $\psi_{\boldsymbol{\kappa}}(\mathbf{r}) = e^{i\mathbf{k} \cdot \mathbf{r}} \phi_{\mathbf{k}_0, \mathbf{k}}(\mathbf{r})$ , with  $\phi_{\mathbf{k}_0, \mathbf{k}}(\mathbf{r}) = e^{i\mathbf{k}_0 \cdot \mathbf{r}} u_{\mathbf{k}_0 + \mathbf{k}}(\mathbf{r})$ , where  $u_{\mathbf{k}_0 + \mathbf{k}}(\mathbf{r}) \equiv u_{\boldsymbol{\kappa}}(\mathbf{r})$  is the periodic part of the Bloch function, while  $\phi_{\mathbf{k}_0, \mathbf{k}}(\mathbf{r})$  carries the phase given by  $\mathbf{k}_0$  and obeys the Schrödinger equation  $[H^0 + H'(\mathbf{k})]\phi_{\mathbf{k}_0, \mathbf{k}}(\mathbf{r}) = [E - k^2]\phi_{\mathbf{k}_0, \mathbf{k}}(\mathbf{r})$ , with

$$H^0 = p^2 + V(\mathbf{r}) + 2\mathbf{k}_0 \cdot \boldsymbol{\pi} + H_{\text{SR}}, \quad (1)$$

$$H'(\mathbf{k}) = 2\mathbf{k} \cdot \boldsymbol{\pi}, \quad (2)$$

$$\boldsymbol{\pi} = \mathbf{p} + \frac{\alpha^2}{8} \boldsymbol{\sigma} \times \nabla V(\mathbf{r}), \quad (3)$$

where  $H^0$  is the Hamiltonian at  $\mathbf{k} = 0$ ,  $H'(\mathbf{k})$  carries the  $\mathbf{k}$ -dependent contributions that will be considered as a perturbation hereafter, and  $\boldsymbol{\pi}$  is the generalized momentum that includes the spin-orbit contributions (SOC). For simplicity, we consider only leading order corrections of the fine structure terms. Namely, at  $\mathbf{k} = 0$ , the  $H_{\text{SR}}$  carries the scalar relativistic terms, composed by the Darwin,  $H_{\text{D}} = \frac{\alpha^2}{8} \nabla^2 V(\mathbf{r})$ , and the mass-velocity corrections,  $H_{\text{MV}} = -\alpha^2 p^4/4$ . In the *ab initio* DFT data, these are implied in the numerical eigenvalues  $E_n^0$  of  $H^0$ . For finite  $\mathbf{k} \neq 0$ , we keep only the SOC contribution in  $\boldsymbol{\pi}$ , and neglect the higher order mass-velocity corrections (see Appendix A).

The DFT data, as shown in the next section, provide us with a set  $\{|n\rangle\}$  of eigenstates of  $H^0$ , i.e.  $H^0 |n\rangle = E_n^0 |n\rangle$ . From these, we define a *crude* all bands model  $H_{\text{all}}^{\text{DFT}}(\mathbf{k})$ , with matrix elements

$$\langle m | H_{\text{all}}^{\text{DFT}} | n \rangle = E_n^0 \delta_{m,n} + 2\mathbf{k} \cdot \mathbf{P}_{m,n}, \quad (4)$$

where  $\mathbf{P}_{m,n} = \langle m | \boldsymbol{\pi} | n \rangle$ . We refer to this as the *crude* model because it is calculated from the original numerical DFT wave-functions, which is does not have an optimal shape (more detail in Section II C). Nevertheless, it already shows that  $E_n^0$  and  $\mathbf{P}_{m,n}$  are central quantities, and both can be extracted from DFT simulations, as shown in Section II D.

Next, we want to fold down  $H_{\text{all}}^{\text{DFT}}$  into a subspace of  $N$  bands near the Fermi energy to obtain our reduced, but still *crude*, effective model  $H_{N \times N}^{\text{DFT}}$ . This is

done via Löwdin partitioning [15, 70]. First, the user must inform the set of  $N$  bands of interest, which we refer as set  $\alpha$ . Complementary, the remaining remote bands compose set  $\beta$ . Considering the diagonal basis  $H^0 |n\rangle = E_n^0 |n\rangle$ , and the perturbation  $H'(\mathbf{k})$ , the Löwdin partitioning leads to the effective Hamiltonian  $H_{N \times N}^{\text{DFT}}$  defined by the expansion

$$\begin{aligned} [H_{N \times N}^{\text{DFT}}]_{m,n}(\mathbf{k}) &= \left( E_n^0 + k^2 \right) \delta_{m,n} + H'_{m,n}(\mathbf{k}) \\ &+ \frac{1}{2} \sum_{r \in \beta} H'_{m,r}(\mathbf{k}) H'_{r,n}(\mathbf{k}) \left( \frac{1}{E_m^0 - E_r^0} + \frac{1}{E_n^0 - E_r^0} \right) + \dots \end{aligned} \quad (5)$$

with  $H'_{m,n}(\mathbf{k}) = \langle m | H'(\mathbf{k}) | n \rangle = 2\mathbf{k} \cdot \mathbf{P}_{m,n}$ . Here, the indices  $m, n \in \alpha$  run over the bands we want to model (set  $\alpha$ ), while  $r \in \beta$  run over the remote bands. The expansion above is shown up to second order in  $H'$ , but higher order terms can be found in Ref. [15].

### B. The optimal shape of $\mathbf{H}$

The selection rules from group theory allow us identify which matrix elements of an effective Hamiltonian are finite [67]. More interestingly, the method of invariants [15, 70] can be used to directly obtain the most general *shape* of  $H_{N \times N}^{\text{optimal}}(\mathbf{k})$  allowed by symmetry. To define this *shape*, consider a Taylor series expansion

$$H_{N \times N}^{\text{optimal}}(\mathbf{k}) = \sum_{i,j,l} h_{i,j,l} k_x^i k_y^j k_z^l, \quad (6)$$

where  $h_{i,j,l}$  are constant matrices that multiply the powers of  $\mathbf{k} = (k_x, k_y, k_z)$  as indicated by its indices  $l, j, k = \{0, 1, 2, \dots\}$ . To find the symmetry allowed  $h_{i,j,l}$ , we recall that the space group  $\mathcal{G}$  of the crystal is defined by symmetry operations that keep the crystalline structure invariant. Particularly, at a high symmetry point  $\boldsymbol{\kappa} = \mathbf{k}_0$ , one must consider the little group  $\mathcal{G}_{\mathbf{k}_0} \in \mathcal{G}$  of symmetry operations that maintain  $\mathbf{k}_0$  invariant (the star of  $\mathbf{k}_0$ ). Hence,  $H_{N \times N}^{\text{optimal}}(\mathbf{k})$  must commute with the symmetry operations of  $\mathcal{G}_{\mathbf{k}_0}$ . Namely

$$H_{N \times N}^{\text{optimal}}(\mathbf{k}) = D^\psi(S) H_{N \times N}^{\text{optimal}}(D^k(S^{-1})\mathbf{k}) D^\psi(S^{-1}), \quad (7)$$

where  $D^\psi(S)$  are the representation matrices for each symmetry operator  $S \in \mathcal{G}_{\mathbf{k}_0}$  in the subspace defined by the wave-functions of set  $\alpha$ , and  $D^k(S)$  are the representation matrices acting on the vector  $\mathbf{k} = (k_x, k_y, k_z)$ . The set of equations defined by this relation for all  $S \in \mathcal{G}_{\mathbf{k}_0}$  leads to a linear system of equations that constrain the symmetry allowed shape of  $H_{N \times N}^{\text{optimal}}(\mathbf{k})$ , i.e., it defines which of constant matrices  $h_{i,j,l}$  are allowed up to a multiplicative factor. Ultimately, these multiplicative factors are the Kane and Luttinger parameters that we want to calculate numerically.

The python package `Qsymm` [65] implements an efficient algorithm to find the *shape* of  $H_{N \times N}^{\text{optimal}}(\mathbf{k})$  solving the equation above and returns the symmetry allowed  $h_{i,j,l}$ . `Qsymm` refers to these as the *Hamiltonian family*. To perform the calculation, the user must inform the representation matrices  $D^\psi(S)$  for the generators of  $\mathcal{G}_{\mathbf{k}_0}$ . Notice that the choice of representation is arbitrary, and different choices lead to effective Hamiltonians with different *shapes*. This ambiguity is the reason why the next step, the symmetry optimization, is necessary.

### C. Symmetry optimization

In the previous section, the matrix representations for generators  $S \in \mathcal{G}_{\mathbf{k}_0}$  are implicitly written in an *optimal* basis, which we will now label with a B index, as in  $\{|n_B\rangle\}$ , to distinguish from the *crude* numerical basis, which we now label with an A index, as in  $\{|n_A\rangle\}$ . The matrix representations of  $S$  written in these two basis are *equivalent* up to an unitary transformation  $U$ , i.e.  $D^B(S) = U \cdot D^A(S) \cdot U^\dagger$ . Indeed, this same matrix  $U$  transforms the *crude* numerical Hamiltonian into the desired *optimal shape*, i.e.  $H_{N \times N}^{\text{optimal}} = U \cdot H_{N \times N}^{\text{DFT}} \cdot U^\dagger$ . Therefore, our goal here is to find this transformation matrix  $U$ .

For each symmetry operator  $S_i \in \mathcal{G}_{\mathbf{k}_0}$ , let us define  $A^i \equiv D^A(S_i)$  and  $B^i \equiv D^B(S_i)$  as the representation matrices under the original numerical DFT basis (A), and under the desired optimal representation (B), respectively. For irreducible representations, this  $U$  is unique (modulo a phase factor) and an efficient method to obtain it was recently developed [64, 71]. Here, however, we propose an alternative method that applies more easily to reducible representations.

The set of unitary transformations  $B^i = U \cdot A^i \cdot U^\dagger$  for each  $S_i \in \mathcal{G}_{\mathbf{k}_0}$  compose a system of equations for  $U$ . These can be written in terms of the its matrix elements in a *linearized* form that reads as

$$\sum_j U_{m,j} A_{j,n}^i - B_{m,j}^i U_{j,n} = 0. \quad (8)$$

Defining a vector  $\mathbf{V} = \{U_{1,1}, U_{1,2}, \dots, U_{2,1}, \dots, U_{N,N}\}^T$ , where  $N$  is the order of the representations (number of bands in set  $\alpha$ ), allow us to cast the equation above as  $\mathbf{Q}_i \cdot \mathbf{V} = 0$ , with  $\mathbf{Q}_i = 1_N \otimes (A^i)^T - B^i \otimes 1_N$  of size  $N^2 \times N^2$ , and  $1_N$  as the  $N \times N$  identity matrix. Since the same similarity transformation  $U$  must apply for all  $S_i$ , we stack each  $\mathbf{Q}_i$  into a rectangular matrix  $\mathbf{Q} = [\mathbf{Q}_1, \mathbf{Q}_2, \dots, \mathbf{Q}_q]^T$  of size  $(qN^2) \times N^2$ . The full set of equations now read as  $\mathbf{Q} \cdot \mathbf{V} = 0$ , such that the solution  $\mathbf{V} = \sum_{j=1}^{N_Q} c_j \mathbf{v}_j$  is a linear combination of the nullspace  $\{\mathbf{v}_j\}$  of  $\mathbf{Q}$ , with coefficients  $c_j$  and nullity  $N_Q$ . The matrix  $U$  can be recovered from the elements of  $\mathbf{V}$ , which follow from its definition above. If  $\mathbf{u}_j$  is the matrix reconstructed form of  $\mathbf{v}_j$ , we can write  $U = \sum_{j=1}^{N_Q} c_j \mathbf{u}_j$ .

Additionally, it is interesting to consider anti-unitary symmetries. These can be either the time-reversal symmetry (TRS) itself, or combinations of TRS and space group operations (magnetic symmetries) [67, 68]. For instance, in spinful graphene neither TRS nor spatial inversion are symmetries of the K point, but their composition is an important symmetry that enforces a constraint on the allowed SOC terms. Following a notation similar to the one above, let us refer to these magnetic symmetries as  $\tilde{A}^i = D^A(\tilde{S}_i)\mathcal{K} \equiv \tilde{A}^i\mathcal{K}$  and  $\tilde{B}^i = D^B(\tilde{S}_i)\mathcal{K} \equiv \tilde{B}^i\mathcal{K}$ , where  $\mathcal{K}$  is the complex conjugation, and  $(\tilde{A}^i, \tilde{B}^i)$  are the unitary parts of  $(\tilde{A}^i, \tilde{B}^i)$ . Now the basis transformation for these symmetries read as  $\tilde{B}^i = U^* \cdot \tilde{A}^i \cdot U^\dagger$ , where we choose to apply  $\mathcal{K}$  to the left (this choice is for compatibility with the python package `IrRep` [69]). To add this equation to the  $\mathbf{Q}$  matrix above, we consider  $U$  and  $U^*$  as independent variables. Then, as above, it follows the *linearized* form

$$\sum_j U_{m,j}^* \tilde{A}_{j,n}^i - \tilde{B}_{m,j}^i U_{j,n} = 0. \quad (9)$$

In all cases, the expression for the transformation matrix is  $U = \sum_{j=1}^{N_Q} c_j \mathbf{u}_j$ , where the coefficients  $c_j$  are arbitrary. Their absolute values  $|c_j|$  are arbitrary due to the linearized form of Eqs. (8) and (9). However, their phases are arbitrary even in the quadratic forms  $B^i = U \cdot A^i \cdot U^\dagger$  and  $\tilde{B}^i = U^* \cdot \tilde{A}^i \cdot U^\dagger$ , which is due to free relative phases between the basis functions of different irreps. For the unitary constraints,  $B^i = U \cdot A^i \cdot U^\dagger$ , the solution  $U$  is invariant under  $U \rightarrow e^{i\theta} U$  for any real  $\theta$ , while for the anti-unitary constraint,  $\tilde{B}^i = U^* \cdot \tilde{A}^i \cdot U^\dagger$ ,  $U$  is invariant only for  $\theta = 0$  or  $\pi$ . This arbitrariness might lead the ill defined phases of matrix elements between basis functions of different irreps if the anti-unitary symmetries are not informed. In contrast, if anti-unitary symmetries are used, the undefined phase factor in the matrix elements is just a sign. In any case, to find the coefficients  $c_j$ , we numerically solve for  $c_j$  by minimizing the residues  $R(\{c_j\}) = \sum_i \|B_i - U \cdot A^i \cdot U^\dagger\|$ , and  $\tilde{R}(\{c_j\}) = \sum_i \|\tilde{B}_i - U^* \cdot \tilde{A}^i \cdot U^\dagger\|$ .

### D. Matrix elements via DFT

As shown above, our approach to obtain a  $\mathbf{k} \cdot \mathbf{p}$  model directly from the DFT data relies on two quantities: (i) the band energies  $E_n^0$  at the  $\mathbf{k} \cdot \mathbf{p}$  expansion point  $\mathbf{k}_0$ ; and (ii) the matrix elements  $\mathbf{P}_{m,n} = \langle m | \boldsymbol{\pi} | n \rangle$  also calculated at  $\mathbf{k}_0$  for all bands  $\{|n\rangle\}$ . The band energies  $E_n^0$  are a straightforward output of any DFT code. Therefore, here we discuss only the calculation of  $\mathbf{P}_{m,n} = \langle m | \boldsymbol{\pi} | n \rangle$ .

We focus on the Quantum Espresso (QE) [3, 4] implementation of *ab initio* DFT [1, 2]. The Hamiltonian in QE is split into the core and inter-core regions via the Projector Augmented Wave (PAW) method [60–62], which is backwards compatible with ultrasoft (USPPs) [61, 72] and norm-conserving pseudo-potentials (NCP) [61, 72]



[73–75]. In these approaches, the atomic core region is replaced by pseudopotentials, which are constructed from single-atom DFT simulations with the Dirac equation in the scalar relativistic or full relativistic approaches. Thus, for molecules or crystals, QE solves a pseudo-Schrödinger equation, with the atomic potentials replaced by the pseudopotentials. Here we shall not go through details of the PAW and pseudopotential methods. For the interested reader, we suggest Refs. [60–62]. Instead, for now, it is sufficient to conceptually understand that QE provides numerical solutions for the Schrödinger equation with the fine structure corrections, which can be expressed by the Hamiltonian

$$H \approx p^2 + V(\mathbf{r}) + H_{\text{SR}} + \frac{\alpha^2}{4}(\boldsymbol{\sigma} \times \nabla V) \cdot \mathbf{p}, \quad (10)$$

where  $H_{\text{SR}} = H_{\text{D}} + H_{\text{MV}}$  contain the Darwin and mass-velocity contributions, as presented above, and the last term is the spin-orbit coupling.

### 1. Matrix elements of the velocity

Fortunately, the QE code already provides tools to calculate the matrix elements of the velocity operator  $\frac{1}{2}\mathbf{v} = \frac{i}{2}[H, \mathbf{r}]$ , which reads as

$$\frac{\mathbf{v}}{2} = \frac{1}{2} \frac{\partial H}{\partial \mathbf{p}} = \boldsymbol{\pi} + \frac{1}{2} \frac{\partial H_{\text{MV}}}{\partial \mathbf{p}} \approx \boldsymbol{\pi}, \quad (11)$$

where we neglect the mass velocity corrections (see Appendix A). Thus, we find that  $\mathbf{P}_{m,n} = \langle m | \boldsymbol{\pi} | n \rangle \approx \langle m | \frac{1}{2}\mathbf{v} | n \rangle$ . The calculation of  $\mathbf{P}_{m,n}$  is already partially included in the post-processing tool `bands.x` (file `PP/src/bands.f90`), within the `write_p_avg` subroutine (file `PP/src/write_p_avg.f90`). This calculation includes the necessary PAW, USPPs, or NCPPs corrections, which are critical for materials where the wavefunction strongly oscillates near the atomic cores [76]. However, the `write_p_avg` subroutine only calculates  $|\mathbf{P}_{m,n}|^2$  for  $m$  in the valence bands (below the Fermi level) and  $n$  in the conduction bands (above the Fermi level). To overcome this limitation, we have built a patch that modifies `bands.f90` and `write_p_avg.f90` to calculate  $\mathbf{P}_{m,n}$  for all bands. This leads to a modified `bands.x` with options to follow with its original behavior, or to calculate  $\mathbf{P}_{m,n}$  accordingly to our needs. This is controlled by a new flag `lpall = False/True` added to the input file of `bands.x` in addition to the `lp = True`. Its default value (`lpall = False`) runs `bands.x` with its original code, while the option `lpall = True` instructs `bands.x` to store all  $\mathbf{P}_{m,n}$  into the file indicated by the input parameter `filp`.

In contrast, if the user prefers not to apply our patch to modify QE, our code can calculate an approximate  $\mathbf{P}_{m,n}$  using only the plane-wave components outputted by the QE code. In this case, we consider that the pseudo-wavefunction is a reasonable approximation for the *all*

*electron* wavefunction, thus neglecting PAW corrections. Under this approximation,  $\mathbf{P}_{m,n}$  will not account for the SOC corrections, i.e. it calculates  $\mathbf{P}_{m,n} \approx \langle m | \mathbf{p} | n \rangle$ . Therefore, it is preferable to patch QE to use the full  $\mathbf{P}_{m,n}$  instead. Nevertheless, within this approximation, the wave-function  $\psi_{n,\mathbf{k}}(\mathbf{r})$  for band  $n$  at quasi-momentum  $\mathbf{k}$ , and  $\mathbf{P}_{m,n}$  read as

$$\psi_{n,\mathbf{k}}(\mathbf{r}) \approx \frac{1}{\sqrt{V}} \sum_{\mathbf{G}} c_n(\mathbf{G}) e^{i(\mathbf{k}+\mathbf{G})\cdot\mathbf{r}}, \quad (12)$$

$$\mathbf{P}_{m,n} \approx \sum_{\mathbf{G}} (\mathbf{k} + \mathbf{G}) c_m^\dagger(\mathbf{G}) c_n(\mathbf{G}), \quad (13)$$

where  $c_n(\mathbf{G})$  are the plane-wave expansion coefficients (spinors in the spinful case),  $V$  is the normalization volume, and  $\mathbf{G}$  are the lattice vectors in reciprocal space. To implement this calculation, and the one shown next, we use the `IrRep` python package [69], since it already have efficient routines to read and manipulate the QE data.

### 2. Matrix elements of the symmetry operators

To calculate the matrix elements of the symmetry operators, it is sufficient to consider  $\psi_{n,\mathbf{k}}(\mathbf{r})$  from Eq. (12). In this case it is safe to neglect PAW corrections, since they must transform identically to the plane-wave parts under the symmetry operations of the crystal space group. For a generic symmetry operation  $S \in \mathcal{G}_{\mathbf{k}_0}$ , its matrix elements read as

$$D_{m,n}^\psi(S) = \sum_{\mathbf{G},\mathbf{G}'} c_m^\dagger(\mathbf{G}') c_n(\mathbf{G}) \int \frac{e^{-i(\mathbf{k}+\mathbf{G}')\cdot\mathbf{r}} e^{-iS^{-1}(\mathbf{k}+\mathbf{G}')\cdot\mathbf{r}}}{V} d^3r. \quad (14)$$

Using the plane-wave orthogonality, one gets

$$D_{m,n}^\psi(S) = \sum_{\mathbf{G}} c_m^\dagger(-\mathbf{k} + S^{-1} \cdot (\mathbf{k} + \mathbf{G})) c_n(\mathbf{G}), \quad (15)$$

where  $S^{-1}$  is the inverse of  $S$ , and  $S^{-1} \cdot (\mathbf{k} + \mathbf{G})$  is its action on the  $(\mathbf{k} + \mathbf{G})$  vector. For instance, if  $S = I$  is the spatial inversion symmetry,  $S^{-1} \cdot (\mathbf{k} + \mathbf{G}) = -\mathbf{k} - \mathbf{G}$ , and  $D_{m,n}^\psi(S) = \sum_{\mathbf{G}} c_m^\dagger(-2\mathbf{k} - \mathbf{G}) c_n(\mathbf{G})$ .

## III. HANDS ON EXAMPLE: GRAPHENE

In this section we present a detailed example and results for spinless graphene. Graphene [77, 78] is nowadays one of the most studied materials due to the discovery of its Dirac-like effective low energy model, which read as  $H = \hbar v_F \boldsymbol{\sigma} \cdot \mathbf{k}$ . Here,  $\boldsymbol{\sigma} = (\sigma_x, \sigma_y, \sigma_z)$  are Pauli matrices acting on the lattice subspace that will be better defined below,  $\mathbf{k} = (k_x, k_y)$  is the quasi-momentum,

and  $v_F$  is the Fermi velocity, which is the unknown coefficient that we want to calculate in this example. For this purpose, in this first example we follow a pedagogical route. First, we present the symmetry characteristics of the graphene lattice and its wave-functions at the K point. Then, we show the results for the representation matrices and Hamiltonian in the *crude* and *optimal* basis to illustrate how the symmetry optimization of Section II C is used to build the optimal Hamiltonians and identify the numerical values for its coefficients. Later, in Section III B we show a step-by-step tutorial on how to run the code. This example was chosen for its simplicity, which allow for a clear discussion of each step. Later, in Section IV we present a summary of examples for other materials of current interest.

Before discussing the details, we summarize the results for the band structure of graphene in Fig. 1, which compares the DFT data with our two main models. The black lines are calculated from the *crude* all bands model from Eq. (4), which include all bands from the DFT data and uses the matrix elements  $P_{m,n}$  in the original *crude* QE/DFT basis without further processing. In contrast, the red lines are the band structure calculated with the folded down Hamiltonian for a set  $\alpha$  composed by the two bands near the Fermi energy that defines the Dirac cone, and considers the symmetry optimization process to properly identify the  $\mathbf{k} \cdot \mathbf{p}$  parameters. This optimal Hamiltonian is shown in Eq. (21) below, and the numerical value for its parameters is shown at *Step 7* in Section III B.

### A. Overview of the theory and symmetry optimization

The crystal structure of graphene is an hexagonal monolayer of carbon atoms, as shown in Figs. 1(a) and 1(b), which is invariant under the P6/mmm space group (#191). However, since its Dirac cone is composed of  $p_z$  orbitals only, it is sufficient to consider the  $C_{6V}$  factor group to describe the lattice. Particularly, at the K point [see Fig. 1(c)], the star of K corresponds to the little group  $C_{3V}$ , which is generated by a 3-fold rotation  $C_3(z)$  and a mirror  $M_y$ . The Dirac bands of graphene are characterized by the irrep  $E$  of  $C_{3V}$  (or irrep  $K_6$  from P6/mmm [79]), which is composed by basis functions  $(xz, yz)$ .

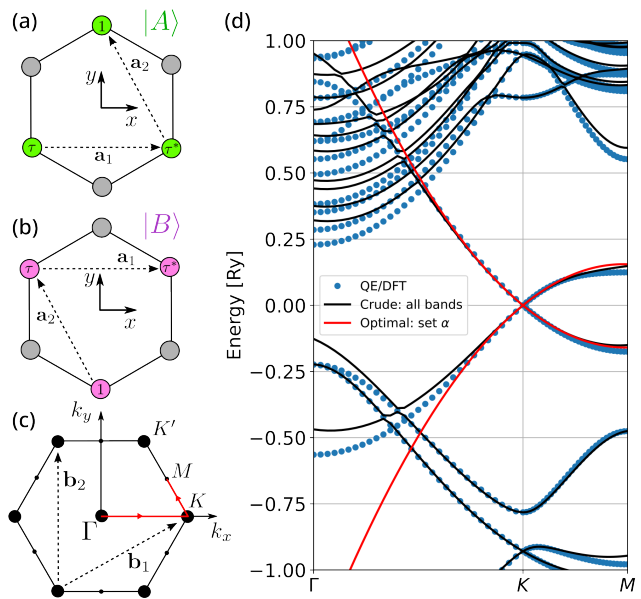


Figure 1. Graphene lattices emphasizing the Dirac cone eigenstates at the K point, where (a)  $|A\rangle = |(X + iY)Z\rangle$  and (b)  $|B\rangle = |(X - iY)Z\rangle$ . Both eigenstates are composed by  $p_z$  orbitals centered at the colored sites (A and B lattices) with the Bloch phase factors indicated within the circles, where  $\tau = \exp(i2\pi/3)$ . (c) The first Brillouin zone marking the path  $\Gamma - K - M$  used to plot the bands in (d). (d) Band structure for graphene calculated via QE/DFT (blue circles), crude all bands model [Eq. (4)] (black lines), and optimal model [Eq. (21)] for the two bands forming the Dirac cone (red). Here, the QE/DFT simulation was performed with 300 bands.

To build the optimal effective model via the method of invariants, we need to specify a basis and calculate the matrix representation of the symmetry operations mentioned above. Since the wave-functions of the Dirac cone transform as the irrep  $E$  of  $C_{3V}$ , a naive choice would be  $\alpha_{\text{unconv}} = \{|XZ\rangle, |YZ\rangle\}$ , which corresponds to a set  $\alpha$  in Section II A. This choice of basis refers to a possible  $B$  representation in Section II C, and it yields

$$D^{\text{unconv}}(C_3(z)) = \begin{pmatrix} \cos \theta & -\sin \theta \\ \sin \theta & \cos \theta \end{pmatrix}, \quad (16)$$

$$D^{\text{unconv}}(M_y) = \begin{pmatrix} 1 & 0 \\ 0 & -1 \end{pmatrix}, \quad (17)$$

$$H_{\text{unconv}} \approx \begin{pmatrix} c_0 - c_1 k_x & c_1 k_y \\ c_1 k_y & c_0 + c_1 k_x \end{pmatrix}, \quad (18)$$

where  $\theta = 2\pi/3$ . Here  $H_{\text{unconv}}$  is obtained via Qsym up to linear order in  $\mathbf{k}$ , for brevity. While the eigenenergies of  $H_{\text{unconv}}$  represent correctly the Dirac cone as  $E_{\pm} = c_0 + |c_1| \sqrt{k_x^2 + k_y^2}$ , the Hamiltonian  $H_{\text{unconv}}$  takes an undesirable unconventional form.

A more convenient choice is  $\alpha_{\text{conv}} = \{|(X + iY)Z\rangle, |(X - iY)Z\rangle\}$ , which is illustrated in

Figs. 1(a) and 1(b). This choice of basis leads to

$$D^{\text{conv}}(C_3(z)) = \begin{pmatrix} e^{i\theta} & 0 \\ 0 & e^{-i\theta} \end{pmatrix}, \quad (19)$$

$$D^{\text{conv}}(M_y) = \begin{pmatrix} 0 & 1 \\ 1 & 0 \end{pmatrix}, \quad (20)$$

$$H_{\text{conv}} \approx \begin{pmatrix} c_0 & c_1 k_- \\ c_1 k_+ & c_0 \end{pmatrix} + \begin{pmatrix} c_2 k_-^2 & c_3 k_+^2 \\ c_3 k_-^2 & c_2 k_+^2 \end{pmatrix}, \quad (21)$$

where  $k_{\pm} = k_x \pm ik_y$ . Now, up to linear order in  $\mathbf{k}$ , we see that  $H_{\text{conv}} \approx c_0 + c_1 \boldsymbol{\sigma} \cdot \mathbf{k}$ , where  $\boldsymbol{\sigma}$  act on the subspace set by  $\alpha_{\text{conv}}$ , and we identify  $c_1 = \hbar v_F$ . Additionally, the k-quadratic terms that lead to trigonal warping corrections. Notice that both choices,  $\alpha_{\text{unconv}}$  and  $\alpha_{\text{conv}}$ , are equivalent representations, but the conventional one leads to the familiar *shape* of the graphene Hamiltonian. These two basis sets are related by a unitary transformation  $U$ , such that  $\alpha_{\text{conv}} = U \alpha_{\text{unconv}}$  and  $H_{\text{conv}} = U H_{\text{unconv}} U^\dagger$ , with

$$U_{\text{unconv} \rightarrow \text{conv}} = \frac{1}{\sqrt{2}} \begin{pmatrix} 1 & i \\ 1 & -i \end{pmatrix}. \quad (22)$$

Next, let us analyze the set  $\alpha_{\text{QE}}$  of numerical wavefunctions from QE. Do they correspond to  $\alpha_{\text{QE}} = \alpha_{\text{conv}}$  or  $\alpha_{\text{QE}} = \alpha_{\text{unconv}}$ ? The answer is neither. Since it is a raw numerical calculation, typically diagonalized via the Davidson algorithm [80], a degenerate or nearly degenerate set of eigenstates might be in any linear combination of its representative basis. Therefore, the symmetry optimization step is essential to find the matrix transformation  $U$  that yields  $\alpha_{\text{conv}} = U \alpha_{\text{QE}}$ . To visualize this, let us check the matrix representations of the symmetry operators above, and the effective Hamiltonian calculated from the *crude* QE data. For the symmetry operators, we find

$$D^{\text{QE}}(C_3(z)) \approx \begin{pmatrix} -0.5 & -0.35 + 0.79i \\ 0.35 + 0.79i & -0.5 \end{pmatrix}, \quad (23)$$

$$D^{\text{QE}}(M_y) \approx \begin{pmatrix} +0.5 & 0.35 - 0.79i \\ 0.35 + 0.79i & -0.5 \end{pmatrix}, \quad (24)$$

While this cumbersome numerical representation does not resemble neither  $\alpha_{\text{conv}}$  nor  $\alpha_{\text{unconv}}$ , our symmetry optimization process correctly finds a transformation matrix  $U$  that returns  $\alpha_{\text{conv}} = U \alpha_{\text{QE}}$ , where

$$U \approx \begin{pmatrix} 0.7i & -0.28 + 0.65i \\ -0.6 + 0.37i & 0.7 - 0.1i \end{pmatrix}. \quad (25)$$

Finally, for the Hamiltonian, up to linear order in  $\mathbf{k}$  and in the original QE basis, we find

$$H_{\text{QE}} \approx \begin{pmatrix} -0.37 & -0.25 + 0.57i \\ -0.25 - 0.57i & 0.37 \end{pmatrix} k_x \\ + \begin{pmatrix} 0.62 & 0.15 - 0.34i \\ 0.15 + 0.34i & 0.62 \end{pmatrix} k_y, \quad (26)$$

which takes a cumbersome *shape* in this raw numerical basis. However, applying the transformation  $U$ , the symmetry adapted model becomes

$$H_{N \times N}^{\text{optimal}} = U H_{N \times N}^{\text{DFT}} U^\dagger \approx 0.72 \boldsymbol{\sigma} \cdot \mathbf{k}. \quad (27)$$

Here we identify  $\hbar v_F = 0.72$  in Rydberg units, yielding  $v_F = 0.83 \times 10^6$  m/s. The resulting band structure calculated from  $H^{\text{optimal}}$ , including the k-quadratic terms, is shown as red lines in Fig. 1(d) and it matches well the QE/DFT data near K.

## B. Running the code

The example presented here is available in the `Examples/graphene-nosoc.ipynb` notebook in the code repository, and shown in Algorithm 1. Here we show only the minimal procedure to read the DFT data, build an effective model from the symmetry constraints, and calculate the numerical values for the model parameters. Complementary, the full code in `Examples/graphene-nosoc.ipynb` shows how to plot the data presented in our figures.

For now, we assume that the DFT simulation was successful. The suggested steps to run QE and prepare the data for our code is to run the `calculation='scf'` and `calculation='bands'` with `pw.x`. Then, run `bands.x` to extract the bands and from QE's output and store it in `gnuplot` format to plot the figures. Here, for graphene, we assume that the `bands` calculation was run for a path  $\Gamma - K - M$  with 30 points between each section, such that K is the 31st point in the list.

Next, we describe each step shown in Algorithm 1.

**Algorithm 1** Minimal example for spinless graphene.

```

1 import numpy as np
2 import pydft2kp as dft2kp
3 # import s0, sx, sy, sz: Pauli matrices
4 from pydft2kp.constants import s0, sx, sy, sz
5
6 # step 1: read DFT data
7 kp = dft2kp.irrep(dftdir='graphene-nosoc',
8                 outdir='outdir',
9                 prefix='graphene',
10                kpt=31,
11                kname='K')
12
13 # step 2: read or calculate matrix elements of p
14 kp.get_p_matrices(qekp='kp.dat')
15
16 # step 3: define the set alpha
17 # applies fold down via Löwdin
18 setA = [3, 4]
19 kp.define_set_A(setA)
20
21 # step 4: builds optimal model with qsymm
22 phi = 2*np.pi/3
23 U = np.diag([np.exp(1j*phi), np.exp(-1j*phi)])
24 C3 = dft2kp.rotation(1/3, [0,0,1], U=U)
25 My = dft2kp.mirror([0,1,0], U=sx)
26 Mz = dft2kp.mirror([0,0,1], U=-s0)
27 TI = dft2kp.PointGroupElement(R=-np.eye(3),
28                               conjugate=True,
29                               U=sx)
30
31 symms = [C3, My, Mz, TI]
32 qs = dft2kp.qsymm(symms, total_power=2, dim=3);
33
34 # step 5: calculate the representation matrices
35 kp.get_symm_matrices()
36 # (optional): adds anti-unitary symmetry
37 kp.add_antiunitary_symm(TI, np.array([0,0,0]))
38
39 # step 6: calculates and applies
40 # the transformation U
41 optimal = dft2kp.basis_transform(qs, kp)
42
43 # step 7: print results
44 optimal.print_report(sigdigits=3)

```

*Step 1.* After running QE, the first step is to read the DFT data from the QE’s output folder. The command `dft2kp.irrep(...)` uses the python package `IrRep` [69] to read the data for the selected  $k$  point to be used in the  $\mathbf{k} \cdot \mathbf{p}$  expansion, as indicated by the parameters `kpt` and `kname`. The data is read from the folder indicated by the parameter `dftdir`, while `outdir` and `prefix` refer to values used in the input file of QE’s `pw.x` calculation. Additionally, the command `dft2kp.irrep(...)` also accepts extra parameters from the package `IrRep` (see code documentation).

*Step 2.* In step 2, the code will either read or calculate the matrix elements  $P_{m,n}$  to build the effective models. If the user runs QE modified by our patch, the QE tool

`bands.x` will generate a file `kp.dat` that already contains the values for  $P_{m,n}$ . In this case, the user must inform the name of this file via the parameter `qekp`. Otherwise, if `qekp` is omitted, our code calculates an approximate value for  $P_{m,n} \approx \langle m | \mathbf{p} | n \rangle$  from the pseudo-wavefunction of QE, as in Eq. (13), which neglects all SOC corrections.

*Step 3.* Next, the user must choose which set of bands will be considered to build the model. This is the set  $\alpha$  in Section II A. In this example we select bands 3 and 4, which correspond to the Dirac cone of graphene. The code analyses the list of bands and identify their irreducible representations (irreps) using the `IrRep` package [69]. Here, the set  $\alpha$  must contain only complete sets of irreps, otherwise the Löwdin perturbation theory would fail with divergences [see Eq. (5)], since the remote bands of set  $\beta$  would have at least one band degenerated with a band from set  $\alpha$ . If this condition fails, the code stops with an error message. Otherwise, if set  $\alpha$  is valid, the code outputs a report indicating the space group of the crystal (e.g., P6/mmm), the selected set of bands (e.g., [3,4]), their irrep (e.g.,  $K_6$  [79]), and degeneracy (2). The report reads as

```

Space group 191 : P6/mmm
Verifying set A: [3 4]
Band indices: [3, 4] Irreps: (K6) Degeneracy: 2

```

Additionally, in this step the code also calculates the *crude* effective model for the bands in set  $\alpha$  via Löwdin partitioning. It stores the folded Hamiltonian in a python dictionary (`kp.Hdict`) representing the matrices  $h_{i,j,l}$  in the QE *crude* basis that define  $H^{\text{DFT}}(\mathbf{k}) = \sum_{i,j,l} h_{i,j,k} k_x^i k_y^j k_z^l$ . For instance, `kp.Hdict['xx']` refers to the matrix  $h_{2,0,0}$  that defines the term  $h_{2,0,0} k_x^2$ .

*Step 4.* In step 4 we build the optimal model using `Qsymm` [65], which solves Eq. (7) for the method of invariants. In Algorithm 1, we build the representations for the symmetry operations  $C_3(z)$ ,  $M_y$ ,  $M_z$ , and  $\mathcal{TI}$ . Above we have discussed only the first two for simplicity. Here we also include the mirror  $M_z$ , and the anti-unitary symmetry  $\mathcal{TI}$ , which is composed by the product of time-reversal and spatial inversion symmetries. The mirror  $M_z$  has a trivial representation  $D^\psi(M_z) = -1$ , since the orbitals that compose the Dirac bands in graphene are all of Z-like (odd in  $z$ ). The  $\mathcal{TI}$  representation follows from  $\alpha_{\text{conv}}$  presented above by recalling that spinless time-reversal is simply the complex conjugation, and the spatial inversion takes  $(X, Y, Z) \rightarrow (-X, -Y, -Z)$ . In this particular example, the  $\mathcal{TI}$  symmetry does not play an important role, but it is essential for a spinful graphene example, as it constrains the SOC terms at finite  $\mathbf{k}$  (see the graphene spinful example in the code repository). The command `dft2kp.qsymm(...)` calls `Qsymm` to build the effective model from the list of symmetries, indicated by `symm`, up to order  $k^2$ , as indicated by `total_power`. We recommend always using `dim=3` [three dimensions for  $\mathbf{k} = (k_x, k_y, k_z)$ ] because QE always work with the 3D space groups. Additionally, the



command `dft2kp.qsymm(...)` accepts other parameters that are passed to the `Qsymm` package (see code documentation). By default, this command outputs the optimal Hamiltonian, which matches the one in Eq. (21).

*Step 5.* Next, we start the symmetry optimization process. The first call `kp.get_symm_matrices()` calculates, via Eq. (15), the matrix representation for all symmetry operators identified in the QE data by the `IrRep` package. However, neither QE nor `IrRep` account for the anti-unitary symmetries. Therefore, we call here the optional routine `kp.add_antiunitary_symm(...)`, which manually adds the anti-unitary symmetry to the list of QE symmetries and match it with the corresponding symmetry of `Qsymm` informed on its first parameter. In this example, we add the  $\mathcal{TI}$  symmetry built with `Qsymm` above. This operator needs to be complemented with a possible non-symmorphic translation vector, which is zero in this case, as shown by the second parameter of `kp.add_antiunitary_symm(...)`. Both calls, `kp.get_symm_matrices()` and `kp.add_antiunitary_symm(...)`, calculate the matrix representations in the *crude* QE basis.

*Step 6.* To calculate the transformation matrix  $U$ , we compare the ideal matrix representations informed via `Qsymm` (object `qs`) and the *crude* QE matrix representations (object `kp`). The call `dft2kp.basis_transform(...)` performs this comparison and returns an error if the symmetries in both objects do not match. More importantly, it calculates the transformation matrix  $U$  solving Eq. (8) and Eq. (9). The matrix  $U$  is stored in the object `optimal.U`. If the calculation of  $U$  is successful, the code applies  $U$  to rotate the  $h_{i,j,l}$  terms in `kp.Hdict` from the *crude* basis into the optimal basis. This allows for a direct identification of the coefficients  $c_n$  from Eq. (21), which are stored in `optimal.coeffs`. Additionally, the code builds the numerical optimal model and provides a callable object `optimal.Heff(kx, ky, kz)` that returns the numerical optimal Hamiltonian  $H_{N \times N}^{\text{optimal}}$  for a given value of  $\mathbf{k} = (k_x, k_y, k_z)$ .

*Step 7.* At last, the code prints a report with the numerical values for the coefficients  $c_n$ , which are summarized in Table (I). As mentioned above, here we identify  $\hbar v_F = 0.72$  a.u., yielding  $v_F = 0.83 \times 10^6$  m/s after converting the units.

Table I. Graphene parameters for the optimal Hamiltonian of Eq. (21).

Coefficient	Values in a.u.	Values in (eV, nm)
$c_0$	$\sim 0$	$\sim 0$ eV
$c_1$	0.72	0.52 eV nm
$c_2$	$\sim 0$	$\sim 0$ eV nm <sup>2</sup>
$c_3$	0.82	0.031 eV nm <sup>2</sup>

## IV. EXAMPLES

In this section we briefly show the results for a series of selected materials without presenting a step-by-step tutorial as above. More detail for each case below can be seen in the code repository. Here we consider examples for zincblende crystals (GaAs, HgTe, CdTe), wurtzite crystals (GaN, GaP, InP), rock-salt crystals (SnTe, PbSe), a transition metal dichalcogenide monolayer (MoS<sub>2</sub>), 3D and 2D topological insulators (Bi<sub>2</sub>Se<sub>3</sub>, GaBiCl<sub>2</sub>). Additional examples can be found in the code repository. In all cases the resulting models agree well with the DFT bands near the  $\mathbf{k} \cdot \mathbf{p}$  expansion point and low energies, as expected. The DFT parameters used in the simulations are presented in Appendix B.

### A. Zincblende crystals

We consider well known zincblende crystals: GaAs, CdTe and HgTe. These crystals are characterized by lattices that transform as the space group  $F\bar{4}3m$ , but their low energy bandstructure concentrates near the  $\Gamma$  point, which can be described by the point group  $T_d$  after factorizing the invariant subgroup of Bloch translations. The basis functions and effective Kane model for these materials are well described in the literature [14, 15, 68]. Here, let us simply summarize this characterization to establish a notation.

In all cases considered in this section, the first conduction band and the top valence bands transform either as  $S$  or  $P = (X, Y, Z)$  orbitals, and in terms of the crystallographic coordinates we define  $x \parallel [100]$ ,  $y \parallel [010]$ , and  $z \parallel [001]$ . In the single group  $T_d$ , neglecting spin, the S-like orbitals transform accordingly to the trivial  $A_1$  irrep of  $T_d$ , while the P-like orbitals transform as the  $T_2$  irrep. Including spin, the double group representation for the S-like orbitals become  $A_1 \otimes D_{1/2} = \bar{\Gamma}_6$ , where  $D_{1/2}$  is the spinor representation, and it yields the spin 1/2 basis functions  $|S \uparrow\rangle$  and  $|S \downarrow\rangle$ . For the P-like bands one gets  $T_2 \otimes D_{1/2} = \bar{\Gamma}_8 \oplus \bar{\Gamma}_7$ , where  $\bar{\Gamma}_8$  represents the basis functions of total angular momentum 3/2, and  $\bar{\Gamma}_7$  has total angular momentum 1/2. These basis functions are listed in Table II. For GaAs and CdTe the conduction band is represented by  $\bar{\Gamma}_6$  (S-type, and spin 1/2), the first valence band is composed by P-type orbitals with total angular momentum 3/2, which are described by the  $\bar{\Gamma}_8$  irrep, and the split-off band contains P-type orbitals with total angular momentum 1/2, which defines the irrep  $\bar{\Gamma}_7$ . In contrast, for HgTe the  $\bar{\Gamma}_6$  and  $\bar{\Gamma}_8$  are inverted due to fine structure corrections.

Table II. Basis functions for zincblende crystals. The first column indicates the double group irreps for the  $T_d$  point group at  $\Gamma$ , which are induced from the single group irreps in parenthesis. The second column lists the basis functions in the basis of total angular momentum, and the third column show their expressions in terms of the symmetry orbitals (S, X, Y, Z) and spin ( $\uparrow$ ,  $\downarrow$ ), which follows the definitions from Ref. [15].

IRREP $T_d$	$ J, m_j\rangle$	orb, spin)
$\bar{\Gamma}_6(A_1)$	$ \frac{1}{2}, +\frac{1}{2}\rangle$	$ S, \uparrow\rangle$
	$ \frac{1}{2}, -\frac{1}{2}\rangle$	$ S, \downarrow\rangle$
$\bar{\Gamma}_8(T_2)$	$ \frac{3}{2}, +\frac{3}{2}\rangle$	$-\frac{1}{\sqrt{2}} X + iY, \uparrow\rangle$
	$ \frac{3}{2}, -\frac{3}{2}\rangle$	$+\frac{1}{\sqrt{2}} X - iY, \downarrow\rangle$
	$ \frac{3}{2}, -\frac{1}{2}\rangle$	$+\frac{1}{\sqrt{6}}[2 Z, \downarrow\rangle +  X - iY, \uparrow\rangle]$
	$ \frac{3}{2}, +\frac{1}{2}\rangle$	$+\frac{1}{\sqrt{6}}[2 Z, \uparrow\rangle -  X + iY, \downarrow\rangle]$
$\bar{\Gamma}_7(T_2)$	$ \frac{1}{2}, -\frac{1}{2}\rangle$	$+\frac{1}{\sqrt{3}}[ Z, \downarrow\rangle -  X - iY, \uparrow\rangle]$
	$ \frac{1}{2}, +\frac{1}{2}\rangle$	$-\frac{1}{\sqrt{3}}[ Z, \uparrow\rangle +  X + iY, \downarrow\rangle]$

The basis from Table II diagonalizes the spinful effective Hamiltonian at  $\mathbf{k} = 0$ , and leads to the well known extended Kane Hamiltonian [15]. The expression for the  $8 \times 8$  Hamiltonian  $H_{ZB}$  is shown in Appendix C in terms of the coefficients  $c_j$  following the output of the `qsymm` code, so that it matches `Examples` in our repository. There, the notation for the powers of  $\mathbf{k}$  follows from Ref. [15], such that it can be directly compared to the extended Kane model shown in their Appendix C. The values for the coefficients  $c_j$  are also shown in Appendix C.

The band structures calculated from  $H_{ZB}$  are shown in Fig. 2, which also shows the crystal lattice and the first Brillouin zone in Figs. 2(a) and 2(b). In all cases, Figs. 2(c-e), the blue dots represent the DFT results. The black lines are the *crude* model from Eq. 4, which includes all DFT bands and approaches a full zone description, but with a cost of a large  $N \times N$  model with typical  $N \gg 100$ . More importantly, the red lines represent effective  $8 \times 8$  Kane model from  $H_{ZB}$ , which matches well the DFT data at low energies and near  $\Gamma$ , as shown in the zoomed insets below each panel for GaAs [Fig. 2(c)], HgTe [Fig. 2(c)], and CdTe [Fig. 2(c)]. Particularly, for HgTe it is clear the band inversion between the  $\bar{\Gamma}_6$  and  $\bar{\Gamma}_8$  irreps.

## B. Wurtzite crystals

The wurtzite crystals form a lattice that is characterized by the space group  $P6_3mc$ , and the low energy band

structure appears near the  $\Gamma$  point only. Near  $\Gamma$ , one can factorize the translations and the resulting factor group is the  $C_{6V}$  point group, which is generated by the  $C_6$  rotation around the  $z$  axis, and the mirror  $M_x$ . Here, in terms of the crystallographic coordinates,  $x \parallel [100]$ ,  $y \parallel [010]$ , and  $z \parallel [001]$ . The unit cell and first Brillouin zone for these materials are shown in Figs. 3(a) and 3(b).

To illustrate the results for wurtzite materials, we consider the cases of GaN, GaP, and InP. Their band structures are shown in Figs. 3(c-e). In all cases, the top valence bands are characterized by the irreps  $(A_1 + E_1) \otimes D_{1/2} = \bar{\Gamma}_7 \oplus 2\bar{\Gamma}_9$ . Here,  $A_1$  is the trivial irrep of  $C_{6V}$  (single group), which represents S-like and Z-like orbitals, and  $E_1$  is the vector representation of  $C_{6V}$  that contains (X, Y)-like orbitals. These are composed with the pure spinor representation  $D_{1/2}$  to define the  $C_{6V}$  double group irreps  $\bar{\Gamma}_7$  and  $\bar{\Gamma}_9$ . Additionally, we consider two conduction bands, which are characterized by the irreps  $(A_1 + B_1) \otimes D_{1/2} = \bar{\Gamma}_8 \oplus \bar{\Gamma}_9$ . The orbital basis function for the  $B_1$  irrep is odd under both  $C_6$  and  $M_x$ , its representation on group character tables is cumbersome, so one defines it as  $|X(X^2 - 3Y^2)\rangle \equiv |V\rangle$  [14]. Ultimately, we consider the double group representations ordered as shown in Table III. There the top indexes  $\{c, v\}$  refer to conduction and valence bands. Notice that the  $\bar{\Gamma}_9$  irrep appears in three pairs of basis functions, which allows for the  $s$ - $p_z$  mixing [81–83]. Here, however, we always work in the diagonal basis ( $H_{WZ}$  is diagonal at  $\mathbf{k} = 0$ ), which is indicated by the primes in the orbitals above. For a recent and detailed discussion on this choice of representation and the  $s$ - $p_z$  mixing, please refer to Ref. [84].

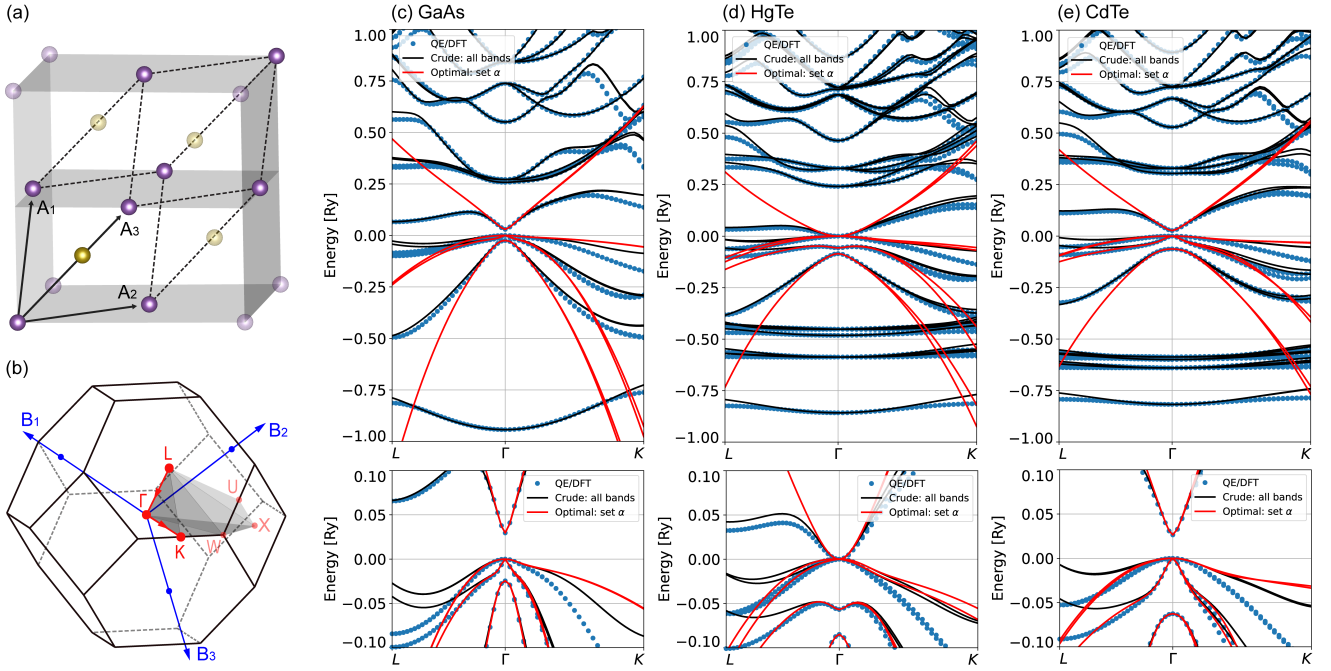


Figure 2. (a) Zincblende lattice, and (b) its first Brillouin zone (FCC). The band structure for (c) GaAs, (d) HgTe, and (e) CdTe are shown over a large energy scale on the main panels, while at the bottom of each panel we show a zoom over the relevant low energy range. In all cases the DFT data consider 1000 bands.

Table III. Basis functions for wurtzite crystals. The first column show the double group irreps of  $C_{6V}$ , which are induced from the single group irrep between parenthesis. The second column show the basis representation in terms of the spherical harmonics  $Y_l^m$  and spin ( $\uparrow, \downarrow$ ), while the third column show the representation in terms of the orbitals (S, X, Y, Z, V), where  $V = X(X^2 - 3Y^2)$  [14].

IRREP $C_{6V}$	$ Y_l^m, \text{spin}\rangle$	$ \text{orb}, \text{spin}\rangle$
$\bar{\Gamma}_9^c(A_1)$	$ Y_0^0, \uparrow\rangle$	$ S', \uparrow\rangle$
	$ Y_0^0, \downarrow\rangle$	$ S', \downarrow\rangle$
$\bar{\Gamma}_8^c(B_1)$	$ Y_3^3 - Y_3^{-3}, \uparrow\rangle$	$ V, \uparrow\rangle$
	$ Y_3^3 - Y_3^{-3}, \downarrow\rangle$	$ V, \downarrow\rangle$
$\bar{\Gamma}_9^v(A_1)$	$ Y_1^0, \uparrow\rangle$	$ Z', \uparrow\rangle$
	$ Y_1^0, \downarrow\rangle$	$ Z', \downarrow\rangle$
$\bar{\Gamma}_9^v(E_1)$	$ Y_1^1, \uparrow\rangle$	$ X' + iY', \uparrow\rangle$
	$ Y_1^{-1}, \downarrow\rangle$	$ X' - iY', \downarrow\rangle$
$\bar{\Gamma}_7^v(E_1)$	$ Y_1^{-1}, \uparrow\rangle$	$ X' - iY', \uparrow\rangle$
	$ Y_1^1, \downarrow\rangle$	$ X' + iY', \downarrow\rangle$

Using the basis functions from Table III to calculate

the effective  $10 \times 10$  model using `qsymm`, we obtain the Hamiltonian  $H_{WZ}$  shown in Appendix C. Here we always consider two conduction bands, which leads to this  $10 \times 10$  generic model  $H_{WZ}$ . However, one can also opt to work with traditional  $8 \times 8$  models with a single conduction band. Notice, however, that for GaP the first conduction band transform as  $\bar{\Gamma}_8$ , while for GaN and InP the first conduction band is  $\bar{\Gamma}_9$ . Therefore, one must be careful when selecting the appropriate  $8 \times 8$  model for wurtzite materials. For the valence bands one always get  $\bar{\Gamma}_7 \oplus 2\bar{\Gamma}_9$ , however, the internal ordering of these valence bands may change between materials and it can be highly sensible to the choice of density functional [85–88]. The numerical coefficients  $c_j$  found for GaN, GaP, InP are shown in Appendix C, and the resulting band structures are shown in Figs. 3(c–e). In all cases we see that the *crude* model with 1000 bands (black lines) approaches a full zone description, but here we are more interested in the reduced  $10 \times 10$  models (red lines), which present satisfactory agreement with the DFT data at low energies.

### C. Rock-salt crystals

The crystal lattice for rock-salt crystals is shown in Fig. 4(a), which is an FCC lattice with two atoms in the base, and it is described by the space group  $Fm\bar{3}m$ . The low energy band structure concentrates at the L point of the Brillouin zone shown in Fig. 4(b), which transforms as the  $D_{3D}$  point group after factorizing the Bloch

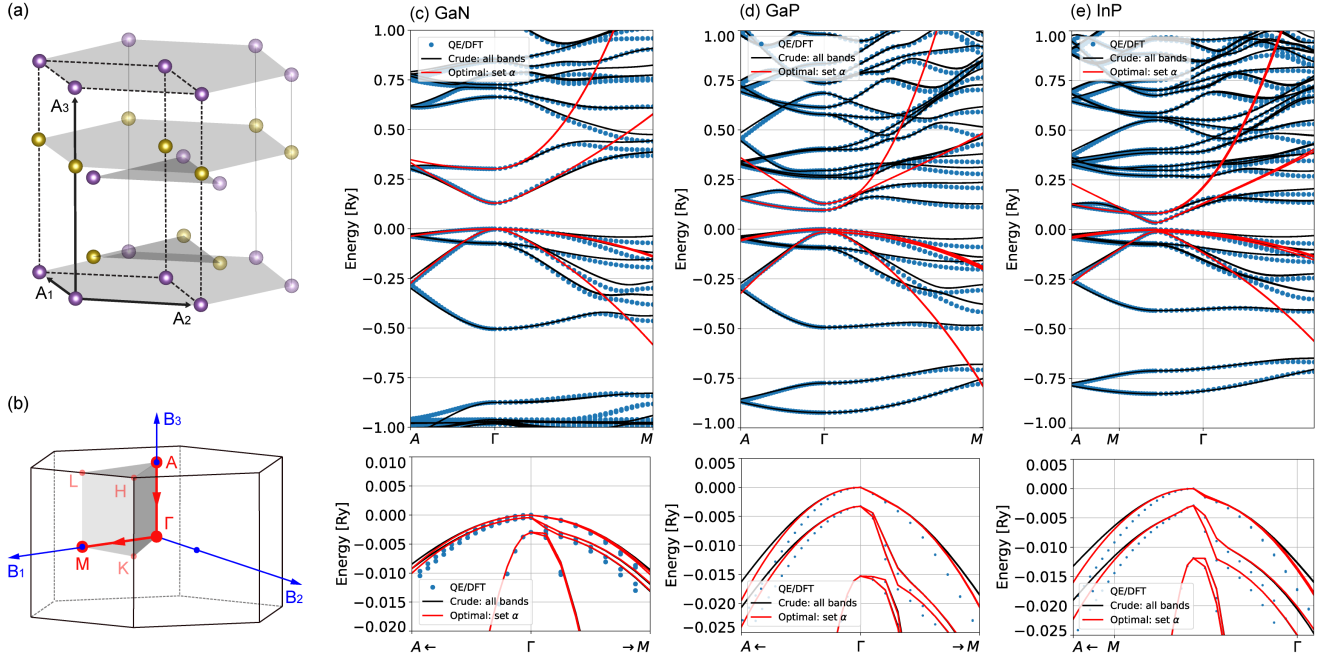


Figure 3. (a) Lattice and (b) Brillouin zone for wurtzite crystals. Band structures for (c) GaN, (d) GaP and (e) InP showing the large energy range on top, and a zoom showing the top of the valence bands at the bottom of each panel. In all cases, the DFT calculation considers 1000 bands.

translations. The basis functions for the first valence and conduction bands transform as  $A_{1g} \otimes D_{1/2} = \bar{L}_6^+$  and  $A_{2u} \otimes D_{1/2} = \bar{L}_6^-$ , where  $A_{1g}$  is the trivial irrep for S-like orbitals, and  $A_{2u}$  represent Z-like orbitals [89]. Therefore, the basis functions for the  $\bar{L}_6^+$  bands are  $\{|S, \uparrow\rangle, |S, \downarrow\rangle\}$ , and for  $\bar{L}_6^-$  one gets  $\{|Z, \uparrow\rangle, |Z, \downarrow\rangle\}$ . Here, the  $x$ ,  $y$ , and  $z$  coordinates are taken along the  $[\bar{1}\bar{1}2]$ ,  $[\bar{1}\bar{1}0]$ , and  $[111]$  crystallographic directions.

Here we consider two examples of rock-salt crystals: PbSe and SnTe. Their effective  $4 \times 4$  Hamiltonian  $H_{RS}$  under the  $\bar{L}_6^\pm$  basis, and its numerical parameters are shown in Appendix C, and the comparison between DFT and model band structures are shown in Figs. 4(c)–(d). PbSe is a narrow gap semiconductor, where the conduction band transform as the  $\bar{L}_6^+$  irrep, and the valence band as  $\bar{L}_6^-$ . In contrast, SnTe show inverted bands, with  $\bar{L}_6^+$  below  $\bar{L}_6^-$ , yielding a topological insulator phase [90, 91]. In both cases the low energy model captures the main features of the bands, including the anisotropy.

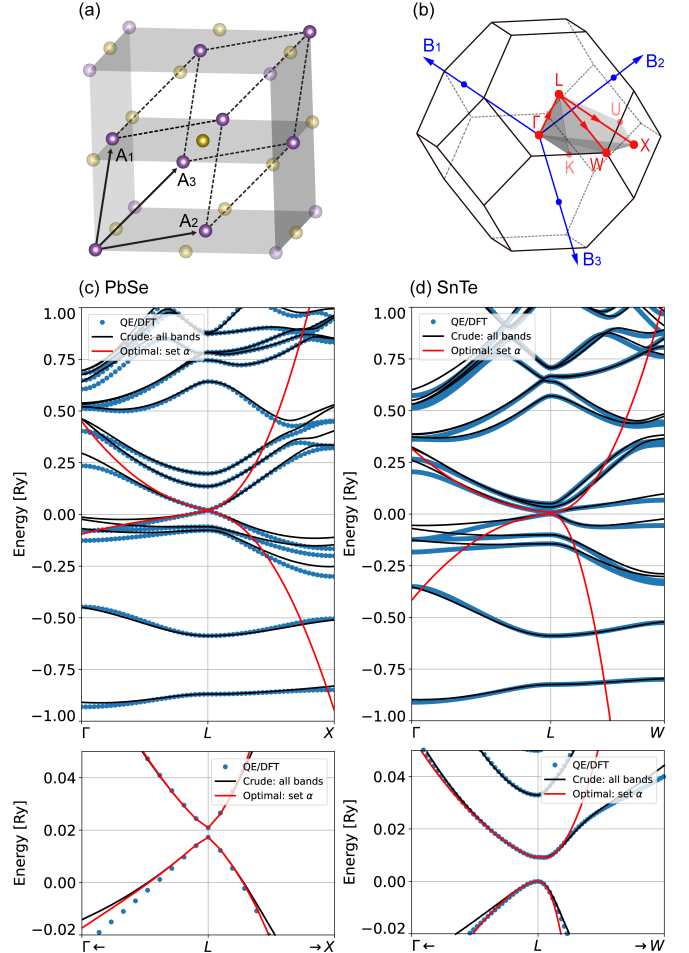


Figure 4. (a) The rock salt lattice and (b) its Brillouin zone (FCC). Band structures for (c) PbSe and (d) SnTe. The bottom of each panel zooms into the low energy range near the Fermi level. Both DFT calculations were performed considering 500 bands.



### D. Other examples

To finish the set of illustrative examples, we show here the case for: (i) the monolayer MoS<sub>2</sub>, which is one of the most studied transition metal dichalcogenides (TMDC) [92–94]; (ii) the bulk bismuth selenide (Bi<sub>2</sub>Se<sub>3</sub>), which is one of the first discovered 3D topological insulators [95, 96]; and (iii) a monolayer of GaBiCl<sub>2</sub>, which is a large gap 2D topological insulator [97].

The symmetry characteristics and basis functions for the low energy bands of these materials mentioned above are summarized in Table IV. For MoS<sub>2</sub>, the first valence and conduction bands are given by the single group irreps  $A'$  and  $E'_1$  of the  $C_{3h}$  group [39, 98], which can be represented as S-like and  $(X + iY)$ -like orbitals. For GaBiCl<sub>2</sub>, the valence bands are characterized by single group  $E$  irrep, and it splits into  $E \otimes D_{1/2} = \bar{\Gamma}_4 \oplus \bar{\Gamma}_5 \oplus \bar{\Gamma}_6$  in the spinful case, while the conduction band is given by the irrep  $A_1 \otimes D_{1/2} = \bar{\Gamma}_6$ . For Bi<sub>2</sub>Se<sub>3</sub>, a detailed derivation of the effective model can be seen in Ref. [99], which shows that the first valence and conduction bands are given by  $A_{1g} \otimes D_{1/2} = \Gamma_6^+$ , and  $A_{2u} \otimes D_{1/2} = \Gamma_6^-$ .

Table IV. Summary of space group, irreps and basis functions for the low energy bands of MoS<sub>2</sub>, GaBiCl<sub>2</sub>, and Bi<sub>2</sub>Se<sub>3</sub>. The first column lists the materials, the second indicates the lattice space group and the little group at the relevant k point. The third and fourth columns lists the irreps and basis functions for the low energy bands in each case. The table show the double group irreps and the corresponding single group irreps between parenthesis.

Material	Group info	IRREP	Basis
MoS <sub>2</sub>	Space group	$\bar{K}_{11}(E'_1)$	$ X + iY, \uparrow\rangle$
	$P\bar{6}m2$	$\bar{K}_{10}(E'_1)$	$ X + iY, \downarrow\rangle$
	Little group	$\bar{K}_8(A')$	$ S, \uparrow\rangle$
	K: $C_{3h}$	$\bar{K}_9(A')$	$ S, \downarrow\rangle$
GaBiCl <sub>2</sub>	Space group	$\bar{\Gamma}_4(E)$	$ X + iY, \uparrow\rangle$
		$\bar{\Gamma}_5(E)$	$ X - iY, \downarrow\rangle$
	$P3m1$	$\bar{\Gamma}_6(E)$	$ X - iY, \uparrow\rangle$
	Little group		$ X + iY, \downarrow\rangle$
	$\Gamma: C_{3v}$	$\bar{\Gamma}_6(A_1)$	$ Z, \uparrow\rangle$
		$ Z, \downarrow\rangle$	
Bi <sub>2</sub> Se <sub>3</sub>	Space group	$\bar{\Gamma}_6^+(A_{1g})$	$ S, \uparrow\rangle$
	$R\bar{3}m$		$ S, \downarrow\rangle$
	Little group	$\bar{\Gamma}_6^-(A_{2u})$	$ Z, \uparrow\rangle$
	$\Gamma: D_{3d}$		$ Z, \downarrow\rangle$

The effective Hamiltonians and its numerical coefficients for these materials can be found in the **Examples** folder of the code repository. Here we show only the comparison between the DFT and model band structures in Fig. 5. The MoS<sub>2</sub> case, as shown in Fig. 5(a), is challenging for a  $\mathbf{k} \cdot \mathbf{p}$  method, since its band structure presents valleys in between high symmetry points. Consequently, the optimal 4 bands model (red lines) captures only the nearly parabolic dispersion at the K point. However, the *crude* all bands model (black lines, see Eq. 4) approaches a full zone description and captures the the valley along the  $\Gamma$ –K direction. For GaBiCl<sub>2</sub>, Fig. 5(c), the optimal 6 bands model describes satisfactorily the low energy conduction and valence bands. For Bi<sub>2</sub>Se<sub>3</sub> in Fig. 5(b) the optimal 4 bands model captures well the low energy band structure near  $\Gamma$ , including the hybridization between the inverted bands.

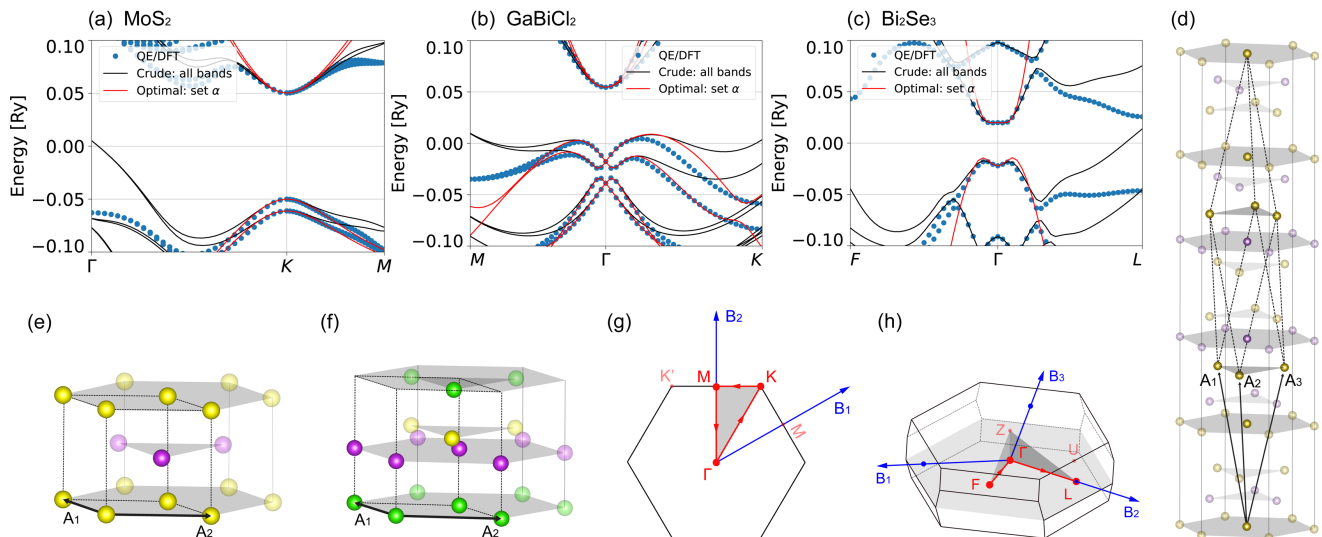


Figure 5. Band structures for: (a) MoS<sub>2</sub>, (b) GaBiCl<sub>2</sub>, and (c) Bi<sub>2</sub>Se<sub>3</sub> showing only the relevant low energy range. The DFT calculations were performed for 1000, 500, 500 bands, respectively. (d) Rhombohedral lattice of Bi<sub>2</sub>Se<sub>3</sub> and 2D hexagonal lattice of (e) MoS<sub>2</sub> and (f) GaBiCl<sub>2</sub>, where we have omitted the vacuum region (15 Å) perpendicular to the plane formed by vectors A<sub>1</sub> and A<sub>2</sub>. (g) 2D Brillouin zone common to MoS<sub>2</sub> and GaBiCl<sub>2</sub>, and (h) 3D BZ of Bi<sub>2</sub>Se<sub>3</sub>.

## V. DISCUSSIONS

Above, we have presented illustrative results of the capabilities of our code to calculate the  $\mathbf{k} \cdot \mathbf{p}$  Kane and Luttinger parameters for a series of relevant materials. In all cases we see a patent agreement between the DFT (QE) data and the low energy models near the relevant  $\mathbf{k}_0$  point. However, it is important to notice that here we use only PBE functionals [100], consequently it often underestimates the gap (e.g. 0.5 eV instead of 1.5 eV for GaAs). Therefore, our models are limited by the quality of the DFT bands, and the resulting numerical parameters might not match Kane and Luttinger parameters for well known materials, for which these parameters are typically chosen to match the experimental data, and not the DFT simulations.

For instance, let us consider the zincblende crystals Kane parameter  $E_P = 2m_0P^2/\hbar^2$ , band gap  $E_g$  and effective mass for the conduction band  $m^*$ . For GaAs, the experimental values are  $E_P \sim 24$  eV,  $P \sim 0.96$  eVnm,  $E_g \sim 1.5$  eV, and  $m^* = 0.065m_0$  [49]. As mentioned above, the DFT results with PBE functionals underestimates the gap, and we get  $E_g \sim 0.5$  eV. Moreover, the Kane parameter can be written as  $P = -\sqrt{6}c_5/2$ , where the coefficient  $c_5 = -0.635$  eVnm is shown in Appendix C. This value yields  $P \sim 0.7$  eVnm and  $E_P \sim 16$  eV. The effective mass for the conduction band can be estimated from its spinless expression [47],  $m_0/m^* = 1 + 2m_0P^2/E_g\hbar^2$ , which give us  $m^* = 0.031m_0$ . While these numbers do not match well with the experimental values, we notice that if we fix the GaAs gap, but keep our value for  $P$ , we find  $m^* = 0.058m_0$ , which is already much closer to the experimental value for the

effective mass.

The number estimates shown above clearly indicates that the quality of our models are limited the DFT simulations only. Particularly, the gap issue can be fixed if one replaces the PBE functionals with hybrid functionals, GW calculations, or other methods that improve the material gap accuracy. These are beyond the scope of this paper, but it is possible path for future improvements of our code.

In all examples presented here, we always consider the *crude* all bands model from Eq. 4, and the optimal (few bands) model from Eq. 5. This raises two interesting questions: (i) how many bands are necessary for convergence? And (ii) for a large number of bands, should we get a full zone description? We discuss these questions below.

### A. Convergence

The convergence threshold (how many bands are necessary) strongly depends on the material. In some cases  $\sim 300$  bands is sufficient, but in others it often needs  $\sim 1000$  bands. We do not have a general rule to establish which materials will show a slow or fast convergence. Nevertheless, we believe it is instructive to discuss the outcomes of our convergence analysis.

Notice that the the Löwdin partitioning from Eq. 5 has two distinct contributions. The first two terms in Eq. 5 are the zeroth and first order perturbation terms. These terms do not change as we increase the number of DFT bands (provided that there are enough bands to converge the DFT calculation itself). The zeroth order

term is essentially given by the DFT eigenstates, and the first order terms is given by the matrix elements  $\langle m | H'(\mathbf{k}) | n \rangle = 2\mathbf{k} \cdot \mathbf{P}_{m,n}$  between eigenstates of set  $\alpha$ , which is the low energy sector of interest. In contrast, the third term defines the second order corrections, which are quadratic in  $\mathbf{k}$  (assuming a diagonal basis at  $\mathbf{k} = 0$ ). In this case, the second order contributions depend explicitly on the sum over the remote set of bands  $\beta$ . These are the terms that strongly depend on the number of remote bands.

To check for the convergence, we plot the values of the Hamiltonian coefficients  $c_j$  associated with second order corrections as a function of the number of remote bands. In the `Examples` folder in the code repository, one finds these plots for all cases presented in this paper. Here, in Fig. 6, we select a few illustrative cases. First, for spinless graphene in Fig. 6(a) there are only three second order  $c_j$  terms, and we see that it reaches convergence near 100 remote bands. In contrast, for MoS<sub>2</sub>, the convergence requires  $\sim 500$  remote bands. Interestingly, it has been recently shown that TMDC materials indeed require a large number of bands to converge the orbital angular momenta [42–45]. This fact may be associated to the large number of unoccupied bands with plane-wave character that appear due to the spatial extension of the vacuum region. The GaN and GaP cases in Figs. 6(c)–(d) is an interesting case, they belong to the same class of materials, but GaP reaches convergence with  $\sim 200$  remote bands, while GaN is not yet fully converged for  $\sim 1000$  remote bands, which can be seen in the lower (pink) line in Fig. 6(c). Surprisingly, unlike monolayer materials, GaN compound is not described by any vacuum region, and therefore we speculate that such poor convergence may be related to details of the pseudopotential [76] and N electronegativity.

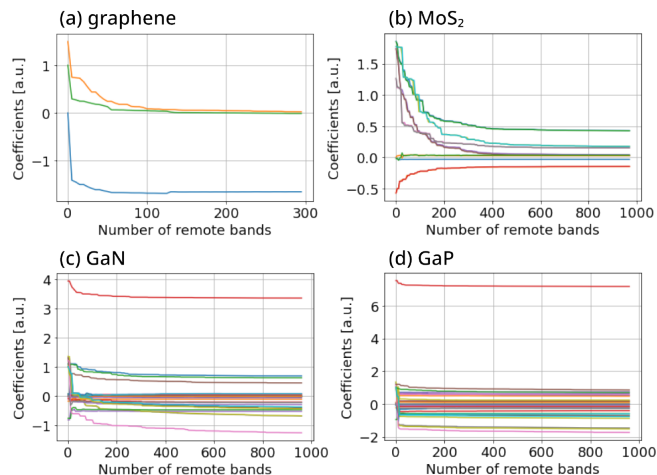


Figure 6. Convergence of the second order coefficients  $c_j$  as a function of the number of remote bands for (a) spinless graphene, (b) MoS<sub>2</sub>, (c) GaN, and (d) GaP. Each line represents a different coefficient  $c_j$  from the Hamiltonian of each material.

## B. Full zone $\mathbf{k} \cdot \mathbf{p}$

In Section II A we have presented the  $\mathbf{k} \cdot \mathbf{p}$  method in its traditional form, which considers a perturbative expansion of the Bloch Hamiltonian at a reference momentum  $\mathbf{k}_0$ , and a small set of bands near the Fermi energy. Usually, one expects the resulting effective model to be valid only near  $\mathbf{k}_0$  and only for a small energy range that encloses the bands of interest. In contrast, within the *full zone*  $\mathbf{k} \cdot \mathbf{p}$  approach [101–106] one considers a large set of bands, such that the resulting low energy model agree well with DFT or experimental bands over the full Brillouin zone, instead of only the vicinity of  $\mathbf{k}_0$ . However, to achieve this precision, one needs to apply fitting procedures to assure that the bands match selected energy levels at various  $\mathbf{k}$  points over the Brillouin zone.

Here, in our code, we can easily select an arbitrary number of bands to build the effective models. All examples presented above show sets of bands colored in red and black, such that the red ones consider models built from a small set of bands  $\alpha$  (from 4 to 10 bands), while the black ones consider the full set of bands from the DFT data (typically 500 or 1000 bands). This leads to an interesting question: should our “all bands model” match the *full zone*  $\mathbf{k} \cdot \mathbf{p}$  models?

To answer this question, let us focus first on the graphene results from Fig. 1. There, we have seen that the QE/DFT and the model agree remarkably well at low energies near the K point, as expected. Particularly, the red line for the optimal model describes precisely the low energy regime and Dirac cone and the trigonal warping from the quadratic terms in Eq. 21. In contrast, when we consider the *crude* all bands model (black lines), we see that the model does approaches a full zone agreement with 300 bands. What if we consider more bands? Our numerical tests have shown that increasing the number of bands does improve the overall description, approaching the *full zone* agreement. However, this is a very slow convergence and we never really reach a true full zone agreement. This characteristic is seen in all other examples shown here.

For GaAs, Gawarecki and collaborators [106] show an excellent full zone agreement between model and DFT bands considering 30 bands. In contrast, our results presented in Fig. 2(a) for 8 (red) and 1000 (black) bands remain valid only in the vicinity of  $\Gamma$ . The key difference is the fitting procedure. The full zone models fit the bands over the full Brillouin zone, while in our approach we consider only the direct *ab-initio* matrix elements of  $\boldsymbol{\pi} = \mathbf{p} + \mathbf{p}_{\text{SOC}}$  without further manipulation.

If one needs a *full zone* model, we suggest using our results as the initial guess for the parameters used on a band fitting algorithm. Moreover, we expect that fitted parameters must not deviate significantly from our *ab-initio* values, which can be used as a “sanity check” for the fitting results. Alternatively, it might be possible to develop multi-valley  $\mathbf{k} \cdot \mathbf{p}$  models [107–109] and extract its parameters directly from DFT matrix elements without

numerical fitting procedures, but this is beyond the scope of this work.

## VI. CONCLUSIONS

We have implemented a numerical framework to calculate the  $\mathbf{k} \cdot \mathbf{p}$  Kane and Luttinger parameters and optimal effective Hamiltonians directly from *ab initio* wavefunctions. The code is mostly written in python, but also contains a patch to modify the Quantum Espresso code, such that its `bands.x` post processing tool is used to calculate the matrix elements  $P_{m,n} = \langle m | \boldsymbol{\pi} | n \rangle$ , which is the central quantity in our methodology. Consequently, this first version works only with Quantum Espresso. Equivalent calculations can be done in other DFT codes (e.g. VASP [5], Wien2k [6]), but it requires further developments. The code is open source and it is available at Ref. [66].

Here, we have illustrated the capabilities of our code applying it to a series of relevant and well known materials. The resulting effective models yield band structures that match well the DFT data in the low energy sector near the  $\mathbf{k}$  point used for the wave-function expansion. Therefore, our code provides an *ab initio* approach for the  $\mathbf{k} \cdot \mathbf{p}$  numerical parameters, which can be contrasted with fitting methods [54–56, 85, 106], in which the numerical coefficients are obtained by numerically minimizing the residue difference between the DFT and model band structures over a selected range of the Brillouin zone. These fitting procedures work well in general, but require a careful verification if the fitted parameters are reasonable. In contrast, our *ab initio* approach is automatic and fully reliable. Nevertheless, fitting procedures can improve the agreement between DFT and model band structures significantly. In this case, we suggest that our code can be used (i) to generate the initial values for the fitting parameters, and (ii) to verify if the fitted parameters show reasonable values. One should expect that fitted parameters must not deviate much from our *ab initio* values.

Here we do not perform a thorough comparison of our numerical parameters with experimental data. Typically, to obtain precise agreement with experimental data, one needs to fix the gap issue by using either hybrid func-

tional or GW calculations, which are beyond the scope of this first version of the code. Instead, here we use only PBE functionals [100] for simplicity, which is reliable enough to validate our approach. Consequently, our numerical parameters are limited by the precision of the DFT simulation, and we would not expect remarkable agreement with experimental data for most materials at this stage. Nevertheless, for novel materials, for which there is no experimental data available, our code can be used to generate reliable numerical parameters that can be improved later, either in comparison with future experiments, or by extending our method to work with hybrid functionals or GW calculations.

As a final disclaimer, we would like to state that after developing the first version of the code, we have found that Ref. [64] recently proposes an equivalent approach to build  $\mathbf{k} \cdot \mathbf{p}$  models from DFT, but the authors do not provide an open source code. In any case, despite the similarities, the development of our code was done independently from their proposal. In practice, the only significant difference between the proposals is the approach to calculate the transformation matrix  $U$  (see Section II C). While the authors of Ref. [64] follow the method from [71], here we propose a different method that is more efficient for transformations involving reducible representations, which is necessary when dealing with nearly degenerate bands of different irreps (e.g., spinful graphene).

## ACKNOWLEDGMENTS

This work was supported by the funding agencies CNPq, CAPES, FAPEMIG. G.J.F. acknowledges funding from the FAPEMIG grant PPM-00798-18). P.E.F.J. acknowledges the financial support of the DFG SFB 1277 (Project-ID 314695032, projects B07 and B11) and SPP 2244 (Project No. 443416183). A.L.A. acknowledges the financial support from FAPESP (grant 2022/08478-6). GFJ acknowledges useful discussions with P. Giannozzi about PAW parameters on QE’s pseudopotentials; H. Zhao for useful discussions and the suggestion to use the `IrRep` and `qeirreps` [110] packages; and S. S. Tsirkin for discussions about the implementation of the `IrRep` package [69].

- 
- [1] P. Hohenberg and W. Kohn, Inhomogeneous electron gas, *Phys. Rev.* **136**, B864 (1964).
  - [2] W. Kohn and L. J. Sham, Self-consistent equations including exchange and correlation effects, *Phys. Rev.* **140**, A1133 (1965).
  - [3] P. Giannozzi, S. Baroni, N. Bonini, M. Calandra, R. Car, C. Cavazzoni, D. Ceresoli, G. L. Chiarotti, M. Cococcioni, I. Dabo, A. D. Corso, S. de Gironcoli, S. Fabris, G. Fratesi, R. Gebauer, U. Gerstmann, C. Gougoussis, A. Kokalj, M. Lazzeri, L. Martin-

- Samos, N. Marzari, F. Mauri, R. Mazzarello, S. Paolini, A. Pasquarello, L. Paulatto, C. Sbraccia, S. Scandolo, G. Sclauzero, A. P. Seitsonen, A. Smogunov, P. Umari, and R. M. Wentzcovitch, QUANTUM ESPRESSO: a modular and open-source software project for quantum simulations of materials, *J. Phys.: Condens. Matter* **21**, 395502 (2009).
- [4] P. Giannozzi, O. Andreussi, T. Brumme, O. Bunau, M. B. Nardelli, M. Calandra, R. Car, C. Cavazzoni, D. Ceresoli, M. Cococcioni, N. Colonna, I. Carnimeo,



- A. D. Corso, S. de Gironcoli, P. Delugas, R. A. DiStasio, A. Ferretti, A. Floris, G. Fratesi, G. Fugallo, R. Gebauer, U. Gerstmann, F. Giustino, T. Gorni, J. Jia, M. Kawamura, H.-Y. Ko, A. Kokalj, E. Küçükbenli, M. Lazzeri, M. Marsili, N. Marzari, F. Mauri, N. L. Nguyen, H.-V. Nguyen, A. O. de-la Roza, L. Paulatto, S. Poncè, D. Rocca, R. Sabatini, B. Santra, M. Schlipf, A. P. Seitsonen, A. Smogunov, I. Timrov, T. Thonhauser, P. Umari, N. Vast, X. Wu, and S. Baroni, Advanced capabilities for materials modelling with quantum ESPRESSO, *J. Phys.: Condens. Matter* **29**, 465901 (2017).
- [5] G. Kresse and J. Furthmüller, Efficient iterative schemes for ab initio total-energy calculations using a plane-wave basis set, *Phys Rev B* **54**, 11169 (1996).
- [6] P. Blaha, K. Schwarz, F. Tran, R. Laskowski, G. K. H. Madsen, and L. D. Marks, WIEN2k: An APW+lo program for calculating the properties of solids, *J. Chem. Phys.* **152**, 074101 (2020).
- [7] M. J. Frisch, G. W. Trucks, H. B. Schlegel, G. E. Scuseria, M. A. Robb, J. R. Cheeseman, G. Scalmani, V. Barone, G. A. Petersson, H. Nakatsuji, X. Li, M. Caricato, A. V. Marenich, J. Bloino, B. G. Janesko, R. Gomperts, B. Mennucci, H. P. Hratchian, J. V. Ortiz, A. F. Izmaylov, J. L. Sonnenberg, D. Williams-Young, F. Ding, F. Lipparini, F. Egidi, J. Goings, B. Peng, A. Petrone, T. Henderson, D. Ranasinghe, V. G. Zakrzewski, J. Gao, N. Rega, G. Zheng, W. Liang, M. Hada, M. Ehara, K. Toyota, R. Fukuda, J. Hasegawa, M. Ishida, T. Nakaajima, Y. Honda, O. Kitao, H. Nakai, T. Vreven, K. Throssell, J. A. Montgomery, Jr., J. E. Peralta, F. Ogliaro, M. J. Bearpark, J. J. Heyd, E. N. Brothers, K. N. Kudin, V. N. Staroverov, T. A. Keith, R. Kobayashi, J. Normand, K. Raghavachari, A. P. Rendell, J. C. Burant, S. S. Iyengar, J. Tomasi, M. Cossi, J. M. Millam, M. Klene, C. Adamo, R. Cammi, J. W. Ochterski, R. L. Martin, K. Morokuma, O. Farkas, J. B. Foresman, and D. J. Fox, Gaussian (2016), gaussian Inc. Wallingford CT.
- [8] B. Hourahine, B. Aradi, V. Blum, F. Bonafè, A. Buccheri, C. Camacho, C. Cevallos, M. Y. Deshayé, T. Dumitrică, A. Dominguez, S. Ehlert, M. Elstner, T. van der Heide, J. Hermann, S. Irle, J. J. Kranz, C. Köhler, T. Kowalczyk, T. Kubař, I. S. Lee, V. Lutsker, R. J. Maurer, S. K. Min, I. Mitchell, C. Negre, T. A. Niehaus, A. M. N. Niklasson, A. J. Page, A. Pecchia, G. Penazzi, M. P. Persson, J. Řezáč, C. G. Sánchez, M. Sternberg, M. Stöhr, F. Stuckenberg, A. Tkatchenko, V. W. z. Yu, and T. Frauenheim, DFTB+, a software package for efficient approximate density functional theory based atomistic simulations, *The Journal of Chemical Physics* **152**, 124101 (2020).
- [9] J. M. Soler, E. Artacho, J. D. Gale, A. García, J. Junquera, P. Ordejón, and D. Sánchez-Portal, The SIESTA method for ab initio order-N materials simulation, *Journal of Physics: Condensed Matter* **14**, 2745 (2002).
- [10] A. García, N. Papior, A. Akhtar, E. Artacho, V. Blum, E. Bosoni, P. Brandimarte, M. Brandbyge, J. I. Cerdá, F. Corsetti, R. Cuadrado, V. Dikan, J. Ferrer, J. Gale, P. García-Fernández, V. M. García-Suárez, S. García, G. Huhs, S. Illera, R. Korytár, P. Koval, I. Lebedeva, L. Lin, P. López-Tarifa, S. G. Mayo, S. Mohr, P. Ordejón, A. Postnikov, Y. Pouillon, M. Pruneda, R. Robles, D. Sánchez-Portal, J. M. Soler, R. Ullah, V. W. zhe Yu, and J. Junquera, Siesta: Recent developments and applications, *The Journal of Chemical Physics* **152**, 204108 (2020).
- [11] J. C. Slater and G. F. Koster, Simplified lcao method for the periodic potential problem, *Phys. Rev.* **94**, 1498 (1954).
- [12] C. M. Goringe, D. R. Bowler, and E. Hernández, Tight-binding modelling of materials, *Reports on Progress in Physics* **60**, 1447 (1997).
- [13] P. Yu and M. Cardona, *Fundamentals of Semiconductors: Physics and Materials Properties*, Advanced texts in physics No. v. 3 (Springer Berlin Heidelberg, 2005).
- [14] M. Willatzen and L. C. L. Y. Voon, *The kp method: electronic properties of semiconductors* (Springer Berlin, Heidelberg, 2009).
- [15] R. Winkler, *Spin-orbit coupling effects in two-dimensional electron and hole systems*, Springer tracts in modern physics (Springer, Berlin, 2003).
- [16] N. Marzari, A. A. Mostofi, J. R. Yates, I. Souza, and D. Vanderbilt, Maximally localized wannier functions: Theory and applications, *Rev. Mod. Phys.* **84**, 1419 (2012).
- [17] M. P. Persson and H. Q. Xu, Giant polarization anisotropy in optical transitions of free-standing InP nanowires, *Phys. Rev. B* **70**, 161310 (2004).
- [18] A. A. Soluyanov, D. Gresch, M. Troyer, R. M. Lutchyn, B. Bauer, and C. Nayak, Optimizing spin-orbit splittings in insb majorana nanowires, *Phys. Rev. B* **93**, 115317 (2016).
- [19] E. Ridolfi, L. R. F. Lima, E. R. Mucciolo, and C. H. Lewenkopf, Electronic transport in disordered  $\text{mos}_2$  nanoribbons, *Phys. Rev. B* **95**, 035430 (2017).
- [20] T. Frank, P. Högl, M. Gmitra, D. Kochan, and J. Fabian, Protected pseudohelical edge states in  $F_2$ -trivial proximitized graphene, *Phys. Rev. Lett.* **120**, 156402 (2018).
- [21] G. Bastard, Superlattice band structure in the envelope-function approximation, *Physical Review B* **24**, 5692 (1981).
- [22] M. G. Burt, An exact formulation of the envelope function method for the determination of electronic states in semiconductor microstructures, *Semiconductor Science and Technology* **2**, 460 (1987).
- [23] M. G. Burt, A new effective-mass equation for microstructures, *Semiconductor Science and Technology* **3**, 1224 (1988).
- [24] G. A. Baraff and D. Gershoni, Eigenfunction-expansion method for solving the quantum-wire problem: Formulation, *Physical Review B* **43**, 4011 (1991).
- [25] M. G. Burt, The justification for applying the effective-mass approximation to microstructures, *Journal of Physics: condensed matter* **4**, 6651 (1992).
- [26] B. A. Foreman, Envelope-function formalism for electrons in abrupt heterostructures with material-dependent basis functions, *Physical Review B* **54**, 1909 (1996).
- [27] C. E. Pryor and M. E. Flatté, Landé  $g$  factors and orbital momentum quenching in semiconductor quantum dots, *Phys. Rev. Lett.* **96**, 026804 (2006).
- [28] T. Campos, P. E. Faria Junior, M. Gmitra, G. M. Sipahi, and J. Fabian, Spin-orbit coupling effects in zincblende insb and wurtzite inas nanowires: Realistic calculations with multiband  $k.p$  method, *Phys. Rev. B* **97**, 245402 (2018).

- [29] J. van Bree, A. Y. Silov, P. M. Koenraad, M. E. Flatté, and C. E. Pryor,  $g$  factors and diamagnetic coefficients of electrons, holes, and excitons in inas/inp quantum dots, *Phys. Rev. B* **85**, 165323 (2012).
- [30] E. G. Novik, A. Pfeuffer-Jeschke, T. Jungwirth, V. Latussek, C. R. Becker, G. Landwehr, H. Buhmann, and L. W. Molenkamp, Band structure of semimagnetic  $\text{Hg}_{1-y}\text{Mn}_y\text{Te}$  quantum wells, *Physical Review B* **72**, 035321 (2005).
- [31] B. A. Bernevig, T. L. Hughes, and S.-C. Zhang, Quantum spin hall effect and topological phase transition in  $\text{HgTe}$  quantum wells, *Science* **314**, 1757 (2006).
- [32] M. S. Miao, Q. Yan, C. G. Van de Walle, W. K. Lou, L. L. Li, and K. Chang, Polarization-driven topological insulator transition in a  $\text{GaN}/\text{InN}/\text{GaN}$  quantum well, *Physical Review Letters* **109**, 186803 (2012).
- [33] M. Holub and B. T. Jonker, Threshold current reduction in spin-polarized lasers: Role of strain and valence-band mixing, *Phys. Rev. B* **83**, 125309 (2011).
- [34] P. E. Faria Junior, G. Xu, J. Lee, N. C. Gerhardt, G. M. Sipahi, and I. Žutić, Toward high-frequency operation of spin lasers, *Phys. Rev. B* **92**, 075311 (2015).
- [35] P. E. Faria Junior and G. M. Sipahi, Band structure calculations of inp wurtzite/zinc-blende quantum wells, *Journal of Applied Physics* **112**, 103716 (2012).
- [36] P. E. Faria Junior, T. Campos, and G. M. Sipahi, Interband polarized absorption in inp polytypic superlattices, *Journal of Applied Physics* **116**, 193501 (2014).
- [37] J. I. Climente, C. Segarra, F. Rajadell, and J. Planelles, Electrons, holes, and excitons in  $\text{GaAs}$  polytype quantum dots, *Journal of Applied Physics* **119**, 125705 (2016).
- [38] P. Li and I. Appelbaum, Electrons and holes in phosphorene, *Physical Review B* **90**, 115439 (2014).
- [39] A. Kormányos, G. Burkard, M. Gmitra, J. Fabian, V. Zólyomi, N. D. Drummond, and V. Fal'ko,  $k$ . $p$  theory for two-dimensional transition metal dichalcogenide semiconductors, *2D Materials* **2**, 049501 (2015).
- [40] P. Li and I. Appelbaum, Symmetry, distorted band structure, and spin-orbit coupling of group-iii metal-monochalcogenide monolayers, *Phys. Rev. B* **92**, 195129 (2015).
- [41] P. E. Faria Junior, M. Kurpas, M. Gmitra, and J. Fabian,  $k$ . $p$  theory for phosphorene: Effective  $g$ -factors, landau levels, and excitons, *Phys. Rev. B* **100**, 115203 (2019).
- [42] T. Woźniak, P. E. Faria Junior, G. Seifert, A. Chaves, and J. Kunstmann, Exciton  $g$  factors of van der waals heterostructures from first-principles calculations, *Physical Review B* **101**, 235408 (2020).
- [43] T. Deilmann, P. Krüger, and M. Rohlfing, Ab initio studies of exciton  $g$  factors: Monolayer transition metal dichalcogenides in magnetic fields, *Physical Review Letters* **124**, 226402 (2020).
- [44] J. Förste, N. V. Tepliakov, S. Y. Kruchinin, J. Lindlau, V. Funk, M. Förg, K. Watanabe, T. Taniguchi, A. S. Baimuratov, and A. Högele, Exciton  $g$ -factors in monolayer and bilayer wse 2 from experiment and theory, *Nature Communications* **11**, 4539 (2020).
- [45] F. Xuan and S. Y. Quek, Valley zeeman effect and landau levels in two-dimensional transition metal dichalcogenides, *Physical Review Research* **2**, 033256 (2020).
- [46] E. Kane, Energy band structure in p-type germanium and silicon, *J. Phys. Chem. Solids* **1**, 82 (1956).
- [47] E. O. Kane, Band structure of indium antimonide, *Journal of Physics and Chemistry of Solids* **1**, 249 (1957).
- [48] J. M. Luttinger and W. Kohn, Motion of electrons and holes in perturbed periodic fields, *Phys Rev* **97**, 869 (1955).
- [49] I. Vurgaftman, J. R. Meyer, and L. R. Ram-Mohan, Band parameters for III-v compound semiconductors and their alloys, *Journal of Applied Physics* **89**, 5815 (2001).
- [50] C. M. O. Bastos, F. P. Sabino, P. E. Faria Junior, T. Campos, J. L. F. D. Silva, and G. M. Sipahi, Stability and accuracy control of  $k \cdot p$  parameters, *Semiconductor Science and Technology* **31**, 105002 (2016).
- [51] P. E. Faria Junior, T. Campos, C. M. O. Bastos, M. Gmitra, J. Fabian, and G. M. Sipahi, Realistic multi-band  $k$ . $p$  approach from ab initio and spin-orbit coupling effects of inas and inp in wurtzite phase, *Phys. Rev. B* **93**, 235204 (2016).
- [52] G. W. Winkler, Q. Wu, M. Troyer, P. Krogstrup, and A. A. Soluyanov, Topological phases in  $\text{inas}_{1-x}\text{sb}_x$ : From novel topological semimetal to majorana wire, *Phys. Rev. Lett.* **117**, 076403 (2016).
- [53] C. M. O. Bastos, F. P. Sabino, G. M. Sipahi, and J. L. F. D. Silva, A comprehensive study of  $g$ -factors, elastic, structural and electronic properties of III-v semiconductors using hybrid-density functional theory, *Journal of Applied Physics* **123**, 065702 (2018).
- [54] A. A. Mostofi, J. R. Yates, Y.-S. Lee, I. Souza, D. Vanderbilt, and N. Marzari, wannier90: A tool for obtaining maximally-localised wannier functions, *Computer Physics Communications* **178**, 685 (2008).
- [55] A. A. Mostofi, J. R. Yates, G. Pizzi, Y.-S. Lee, I. Souza, D. Vanderbilt, and N. Marzari, An updated version of wannier90: A tool for obtaining maximally-localised wannier functions, *Computer Physics Communications* **185**, 2309 (2014).
- [56] M. B. Nardelli, F. T. Cerasoli, M. Costa, S. Curtarolo, R. D. Gennaro, M. Fornari, L. Liyanage, A. R. Supka, and H. Wang, PAOFLOW: A utility to construct and operate on ab initio hamiltonians from the projections of electronic wavefunctions on atomic orbital bases, including characterization of topological materials, *Computational Materials Science* **143**, 462 (2018).
- [57] D. Gresch, Q. Wu, G. W. Winkler, R. Häuselmann, M. Troyer, and A. A. Soluyanov, Automated construction of symmetrized wannier-like tight-binding models from ab initio calculations, *Physical Review Materials* **2**, 103805 (2018).
- [58] C. J. Pickard and M. C. Payne, Second-order  $kp$  perturbation theory with vanderbilt pseudopotentials and plane waves, *Physical Review B* **62**, 4383 (2000).
- [59] T. Shishidou and T. Oguchi,  $kp$  formula for use with linearized augmented plane waves, *Physical Review B* **78**, 245107 (2008).
- [60] P. E. Blöchl, Projector augmented-wave method, *Phys Rev B* **50**, 17953 (1994).
- [61] G. Kresse and D. Joubert, From ultrasoft pseudopotentials to the projector augmented-wave method, *Phys Rev B* **59**, 1758 (1999).
- [62] A. D. Corso, Projector augmented-wave method: Application to relativistic spin-density functional theory, *Phys Rev B* **82**, 075116 (2010).
- [63] P. Schwerdtfeger, The pseudopotential approximation in electronic structure theory, *ChemPhysChem* **12**, 3143

- (2011).
- [64] M. Jocić and N. Vukmirović, Ab initio construction of symmetry-adapted kp hamiltonians for the electronic structure of semiconductors, *Phys Rev B* **102**, 085121 (2020).
- [65] D. Varjas, T. Ö. Rosdahl, and A. R. Akhmerov, Qsymm: algorithmic symmetry finding and symmetric hamiltonian generation, *New J. Phys.* **20**, 093026 (2018).
- [66] The DFT2kp code is available at [gitlab.com/dft2kp/dft2kp](https://github.com/dft2kp/dft2kp).
- [67] M. Tinkham, *Group theory and quantum mechanics* (Dover Publications, 2003).
- [68] M. Dresselhaus, G. Dresselhaus, and A. Jorio, *Group Theory: Application to the Physics of Condensed Matter*, SpringerLink: Springer e-Books (Springer Berlin Heidelberg, 2007).
- [69] M. Iraola, J. L. Mañes, B. Bradlyn, M. K. Horton, T. Neupert, M. G. Vergniory, and S. S. Tsirkin, IrRep: Symmetry eigenvalues and irreducible representations of ab initio band structures, *Comput. Phys. Commun.* **272**, 108226 (2022).
- [70] J. M. Luttinger, Quantum theory of cyclotron resonance in semiconductors: General theory, *Phys Rev* **102**, 1030 (1956).
- [71] M. Mozrymas, M. Studziński, and M. Horodecki, Explicit constructions of unitary transformations between equivalent irreducible representations, *J. Phys. A: Math. Theor.* **47**, 505203 (2014).
- [72] D. Vanderbilt, Soft self-consistent pseudopotentials in a generalized eigenvalue formalism, *Phys Rev B* **41**, 7892 (1990).
- [73] D. R. Hamann, M. Schlüter, and C. Chiang, Norm-conserving pseudopotentials, *Phys. Rev. Lett.* **43**, 1494 (1979).
- [74] G. B. Bachelet, D. R. Hamann, and M. Schlüter, Pseudopotentials that work: From h to pu, *Phys Rev B* **26**, 4199 (1982).
- [75] D. R. Hamann, Optimized norm-conserving vanderbilt pseudopotentials, *Phys Rev B* **88**, 085117 (2013).
- [76] H. Kageshima and K. Shiraishi, Momentum-matrix-element calculation using pseudopotentials, *Phys Rev B* **56**, 14985 (1997).
- [77] K. S. Novoselov, A. K. Geim, S. V. Morozov, D. Jiang, Y. Zhang, S. V. Dubonos, I. V. Grigorieva, and A. A. Firsov, Electric field effect in atomically thin carbon films, *Science* **306**, 666 (2004).
- [78] K. S. Novoselov, D. Jiang, F. Schedin, T. J. Booth, V. V. Khotkevich, S. V. Morozov, and A. K. Geim, Two-dimensional atomic crystals, *Proceedings of the National Academy of Sciences* **102**, 10451 (2005).
- [79] L. Elcoro, B. Bradlyn, Z. Wang, M. G. Vergniory, J. Cano, C. Felser, B. A. Bernevig, D. Orobengoa, G. de la Flor, and M. I. Aroyo, Double crystallographic groups and their representations on the Bilbao crystallographic server, *J. Appl. Crystallogr.* **50**, 1457 (2017).
- [80] E. R. Davidson, The iterative calculation of a few of the lowest eigenvalues and corresponding eigenvectors of large real-symmetric matrices, *J. Comput. Phys.* **17**, 87 (1975).
- [81] E. Rashba, Symmetry of energy bands in crystals of wurtzite type. 1. symmetry of bands disregarding spin-orbit interaction, *Soviet Physics-Solid State* **1**, 368 (1959).
- [82] L. C. L. Y. Voon, M. Willatzen, M. Cardona, and N. E. Christensen, Terms linear in k in the band structure of wurtzite-type semiconductors, *Physical Review B* **53**, 10703 (1996).
- [83] V. Litvinov, *Wide Bandgap Semiconductor Spintronics* (CRC Press, 2016).
- [84] J. Fu, P. H. Penteado, D. R. Candido, G. J. Ferreira, D. P. Pires, E. Bernardes, and J. C. Egues, Spin-orbit coupling in wurtzite heterostructures, *Phys Rev B* **101**, 134416 (2020).
- [85] P. E. Faria Junior, T. Campos, C. M. O. Bastos, M. Gmitra, J. Fabian, and G. M. Sipahi, Realistic multi-band kp approach from ab initio and spin-orbit coupling effects of inas and inp in wurtzite phase, *Phys. Rev. B* **93**, 235204 (2016).
- [86] T. Campos, P. E. Faria Junior, M. Gmitra, G. M. Sipahi, and J. Fabian, Spin-orbit coupling effects in zincblende insb and wurtzite inas nanowires: Realistic calculations with multiband  $\mathbf{k} \cdot \mathbf{p}$  method, *Phys. Rev. B* **97**, 245402 (2018).
- [87] B. C. da Silva, O. D. D. Couto, H. T. Obata, M. M. de Lima, F. D. Bonani, C. E. de Oliveira, G. M. Sipahi, F. Iikawa, and M. A. Cotta, Optical absorption exhibits pseudo-direct band gap of wurtzite gallium phosphide, *Scientific Reports* **10**, 10.1038/s41598-020-64809-4 (2020).
- [88] F. D. Bonani, A. H. Siqueira, H. W. L. Alves, and G. M. Sipahi, *Strain and crystal field splitting inversion in iiii-nitrides* (2021).
- [89] D. L. Mitchell and R. F. Wallis, Theoretical energy-band parameters for the lead salts, *Phys Rev* **151**, 581 (1966).
- [90] T. H. Hsieh, H. Lin, J. Liu, W. Duan, A. Bansil, and L. Fu, Topological crystalline insulators in the snite material class, *Nature communications* **3**, 982 (2012).
- [91] Y. Ando and L. Fu, Topological crystalline insulators and topological superconductors: From concepts to materials, *Annu. Rev. Condens. Matter Phys.* **6**, 361 (2015).
- [92] L. F. Mattheiss, Band structures of transition-metal-dichalcogenide layer compounds, *Physical Review B* **8**, 3719 (1973).
- [93] D. Xiao, G.-B. Liu, W. Feng, X. Xu, and W. Yao, Coupled spin and valley physics in monolayers of mos<sub>2</sub> and other group-vi dichalcogenides, *Physical review letters* **108**, 196802 (2012).
- [94] S. Manzeli, D. Ovchinnikov, D. Pasquier, O. V. Yazyev, and A. Kis, 2d transition metal dichalcogenides, *Nature Reviews Materials* **2**, 1 (2017).
- [95] H. Zhang, C.-X. Liu, X.-L. Qi, X. Dai, Z. Fang, and S.-C. Zhang, Topological insulators in bi<sub>2</sub>se<sub>3</sub>, bi<sub>2</sub>te<sub>3</sub> and sb<sub>2</sub>te<sub>3</sub> with a single dirac cone on the surface, *Nature physics* **5**, 438 (2009).
- [96] Y. Xia, D. Qian, D. Hsieh, L. Wray, A. Pal, H. Lin, A. Bansil, D. Grauer, Y. S. Hor, R. J. Cava, *et al.*, Observation of a large-gap topological-insulator class with a single dirac cone on the surface, *Nature physics* **5**, 398 (2009).
- [97] L. Li, X. Zhang, X. Chen, and M. Zhao, Giant topological nontrivial band gaps in chloridized gallium bismuthide, *Nano Letters* **15**, 1296 (2015).
- [98] D. V. Rybkovskiy, I. C. Gerber, and M. V. Durnev, Atomically inspired kp approach and valley zeeman effect in transition metal dichalcogenide monolayers, *Phys Rev B* **95**, 155406 (2017).

- [99] C.-X. Liu, X.-L. Qi, H. Zhang, X. Dai, Z. Fang, and S.-C. Zhang, Model hamiltonian for topological insulators, *Physical Review B* **82**, 045122 (2010).
- [100] J. P. Perdew, K. Burke, and M. Ernzerhof, Generalized gradient approximation made simple, *Phys. Rev. Lett.* **77**, 3865 (1996).
- [101] M. Cardona and F. H. Pollak, Energy-band structure of germanium and silicon: The k-p method, *Physical Review* **142**, 530 (1966).
- [102] S. B. Radhia, S. Ridene, K. Boujdaria, H. Bouchriha, and G. Fishman, Band structures of ge and InAs: A 20 k.p model, *Journal of Applied Physics* **92**, 4422 (2002).
- [103] R. Beresford, Full-zone k-p method of band structure calculation for wurtzite semiconductors, *Journal of Applied Physics* **95**, 6216 (2004).
- [104] I. Saïdi, S. B. Radhia, and K. Boujdaria, Band structures of GaAs, InAs, and InP: A 34 k-p model, *Journal of Applied Physics* **104**, 023706 (2008).
- [105] I. Saïdi, S. B. Radhia, and K. Boujdaria, Band parameters of GaAs, InAs, InP, and InSb in the 40-band k-p model, *Journal of Applied Physics* **107**, 043701 (2010).
- [106] K. Gawarecki, P. Scharoch, M. Wiśniewski, J. Ziemnicki, H. S. Mączko, M. Gładysiewicz, and R. Kudrawiec, Invariant expansion of the 30-band kp model and its parameters for III-V compounds, *Phys Rev B* **105**, 045202 (2022).
- [107] C. Persson and C. Ambrosch-Draxl, A full-band - method for solving the kohn-sham equation, *Computer Physics Communications* **177**, 280 (2007).
- [108] A. Marnetto, M. Penna, and M. Goano, An accurate dual-expansion-point full-brillouin-zone k-p model for wurtzite semiconductors, *Journal of Applied Physics* **108**, 033701 (2010).
- [109] K. Berland and C. Persson, Enabling accurate first-principle calculations of electronic properties with a corrected kp scheme, *Computational Materials Science* **134**, 17 (2017).
- [110] A. Matsugatani, S. Ono, Y. Nomura, and H. Watanabe, qeirreps: An open-source program for quantum ESPRESSO to compute irreducible representations of bloch wavefunctions, *Computer Physics Communications* **264**, 107948 (2021).
- [111] ONCV pseudopotentials for Quantum Espresso are available at [github.com/pipidog/ONCVSP](https://github.com/pipidog/ONCVSP).

### Appendix A: Mass-velocity corrections are negligible

Consider the full Hamiltonian with all fine structure corrections as

$$H = p^2 + V(r) + H_{\text{MV}} + H_{\text{D}} + H_{\text{SOC}}, \quad (\text{A1})$$

$$H_{\text{MV}} = -\frac{\alpha^2 p^4}{4}, \quad (\text{A2})$$

$$H_{\text{D}} = \frac{\alpha^2}{8} \nabla^2 V, \quad (\text{A3})$$

$$H_{\text{SOC}} = \frac{\alpha^2}{4} (\boldsymbol{\sigma} \times \nabla U) \cdot \mathbf{p}. \quad (\text{A4})$$

Applying the Bloch theorem  $\psi_{\boldsymbol{\kappa}}(\mathbf{r}) = e^{i\mathbf{k} \cdot \mathbf{r}} \phi_{\mathbf{k}_0, \mathbf{k}}(\mathbf{r})$  for  $\boldsymbol{\kappa} = \mathbf{k}_0 + \mathbf{k}$ , the  $\mathbf{k} \cdot \mathbf{p}$  Hamiltonian becomes  $H_{\text{kp}} = H_0 + k^2 + H'$ , where  $H_0 = p^2 + V(\mathbf{r}) + 2\mathbf{k}_0 \cdot \boldsymbol{\pi} + H_{\text{SR}}$ , and

$H_{\text{SR}}$  contain the  $\mathbf{k} = 0$  contributions from  $H_{\text{MV}} + H_{\text{D}}$ , as presented in the main text. The perturbation for finite  $\mathbf{k} \neq 0$  is  $H' = 2\mathbf{k} \cdot \boldsymbol{\pi} + H'_{\text{MV}}$ , where  $H'_{\text{MV}}$  contains the finite  $\mathbf{k}$  contributions from the mass velocity term, and it reads as

$$H'_{\text{MV}} = -\frac{\alpha^2}{4} \left[ 4(\mathbf{k} \cdot \mathbf{p})p^2 + 4(\mathbf{k} \cdot \mathbf{p})^2 + 4(k)^2(\mathbf{k} \cdot \mathbf{p}) + 2k^2p^2 + k^4 \right]. \quad (\text{A5})$$

These corrections are negligible for small  $\mathbf{k}$ , i.e.  $|H'_{\text{MV}}| \ll |2\mathbf{k} \cdot \boldsymbol{\pi}|$ . Notice that the SOC term in  $2\mathbf{k} \cdot \boldsymbol{\pi}$  has two contributions, one is of order  $\sim |kp|$  and the other is  $\sim |k\alpha^2|$ . In contrast, the contributions to  $H'_{\text{MV}}$  are  $\sim |\alpha^2 kp^3|$ ,  $\sim |\alpha^2 k^2 p^2|$ ,  $\sim |\alpha^2 k^3 p|$ , and  $\sim |\alpha^2 k^4|$ . Therefore, all terms in  $H'_{\text{MV}}$  are of higher order than those in  $2\mathbf{k} \cdot \boldsymbol{\pi}$ , and we can safely assume  $H' \approx 2\mathbf{k} \cdot \boldsymbol{\pi}$ .

### Appendix B: DFT parameters

The first principles calculations are performed using the density functional theory (DFT) [1, 2] within the generalized gradient approximation (GGA) for the exchange and correlation functional, employing the Perdew-Burke-Ernzerhof (PBE) parametrization [100]. We employ the non-collinear spin-DFT formalism self-consistently with fully relativistic j-dependent ONCV (Optimized Norm-Conserving Vanderbilt) pseudopotential [75]. The Quantum Espresso (QE) package [3, 4] was used, with a plane waves base configured with a given cut-off energy and the Brillouin zone sampled with a number of k-points (Monkhorst-Pack grid) so that the total energy converged within the meV scale (see Table V). The ONCV pseudopotentials compatible with Quantum espresso package are available in the repository [111]. The vacuum space in two-dimensional materials was set to 15 Å. Atomic structures were optimized with a criterion that requires the force on each atom being less than 0.01 eV/Å. Additional parameters used in our simulations including QE input and output files can be found in the `Examples` folder of the code repository [66].

### Appendix C: Effective Hamiltonians and coefficients

Here we present the large Hamiltonians and table of parameters for the materials presented in the main text. These correspond to the zincblende crystals for Fig. 2, wurtzite crystals of Fig. 3, and rock-salt crystals of Fig. 4. For the other examples shown in Fig. 5, the corresponding Hamiltonians and numerical parameters can be seen in `Examples` folder in the code repository.

The numerical coefficients for the zincblende, wurtzite and rock-salt materials are shown in Tables VI, VII, and VIII, respectively. These correspond to the effective Hamiltonians shown in Tables IX, X, and XI. In all cases we use  $k_{\pm} = k_x \pm ik_y$ ,  $k^2 = k_x^2 + k_y^2 + k_z^2$ ,



Table V. Criteria used for the convergence of the total energy: cut-off energy for the expansion in plane waves and the number of k-points taken for sampling the Brillouin zone using the Monkhorst-Pack technique.

Material	cut-off energy	BZ sample
Graphene	80 Ry	12x12x1
GaAs	100 Ry	8x8x8
HgTe	50 Ry	8x8x8
CdTe	60 Ry	8x8x8
GaN	100 Ry	8x8x8
GaP	150 Ry	8x8x8
InP	100 Ry	7x7x7
PbSe	100 Ry	7x7x7
SnTe	100 Ry	8x8x8
MoS <sub>2</sub>	100 Ry	8x8x1
Bi <sub>2</sub> Se <sub>3</sub>	60 Ry	7x7x7
GaBiCl <sub>2</sub>	100 Ry	8x8x1

$k_{\parallel}^2 = k_x^2 + k_y^2$ ,  $\hat{K} = k_x^2 - k_y^2$ , which is also used in Appendix C of Ref. [15].

Table VI. Table of parameters for the zincblende materials, where the coefficients  $c_n$  refer to the terms of  $H_{ZB}$  in the equation listed in Table IX. The coefficient  $c_0$  is negative for HgTe due to the  $\Gamma_6$ - $\Gamma_8$  band inversion.

Zincblende	GaAs	HgTe	CdTe
$c_0$ (eV)	0.403	-1.16	0.36
$c_1$ (eV)	0.00011	2.23e-05	3.68e-05
$c_2$ (eV)	-0.335	-0.773	-0.851
$c_3$ (eV nm)	0.000486	-0.0117	0.00232
$c_4$ (eV nm)	0.00268	-0.023	0.00499
$c_5$ (eV nm)	-0.635	-0.543	0.559
$c_6$ (eV nm)	-0.436	0.341	0.363
$c_7$ (eV nm <sup>2</sup> )	0.0293	0.0354	0.0347
$c_8$ (eV nm <sup>2</sup> )	-0.0978	-0.0772	-0.0577
$c_9$ (eV nm <sup>2</sup> )	-0.0437	-0.0339	-0.0262
$c_{10}$ (eV nm <sup>2</sup> )	-0.0321	0.0128	-0.0153
$c_{11}$ (eV nm <sup>2</sup> )	-0.0608	-0.0375	-0.0303
$c_{12}$ (eV nm <sup>2</sup> )	-0.000588	-0.0036	-0.000109
$c_{13}$ (eV nm <sup>2</sup> )	0.0632	0.0558	0.0398
$c_{14}$ (eV nm <sup>2</sup> )	0.0397	-0.0259	0.0231
$c_{15}$ (eV nm <sup>2</sup> )	-0.0362	0.0479	0.0361
$c_{16}$ (eV nm <sup>2</sup> )	-0.0275	-0.0349	0.0261

Table VII. Table of parameters for the wurtzite materials, where the coefficients  $c_n$  refer to the terms of  $H_{WZ}$  in the equation listed in Table X.

Wurtzite	GaP	GaN	InP
$c_0$ (eV)	1.75	1.76	0.457
$c_1$ (eV)	9.73e-06	-1.16e-07	1.4e-07
$c_2$ (eV)	-6.28e-06	-5.09e-09	-4.07e-06
$c_3$ (eV)	1.31	4.11	1.1
$c_4$ (eV)	-0.208	-0.0405	-0.162
$c_5$ (eV)	4.7e-08	0.000658	6.89e-09
$c_6$ (eV)	-0.0442	-0.00602	-0.0395
$c_7$ (eV)	7.82e-05	-7.29e-05	8.11e-05
$c_8$ (eV nm)	0.00448	0.00586	-0.0112
$c_9$ (eV nm)	0.00214	0.00075	0.0137
$c_{10}$ (eV nm)	0.118	-0.0733	-0.184
$c_{11}$ (eV nm)	0.455	-0.372	-0.392
$c_{12}$ (eV nm)	-0.472	-0.381	0.436
$c_{13}$ (eV nm)	-0.00429	-0.00428	-0.0195
$c_{14}$ (eV nm)	0.00811	0.0024	0.0223
$c_{15}$ (eV nm)	0.0234	0.0128	0.0301
$c_{16}$ (eV nm)	-0.0268	0.0134	-0.0428
$c_{17}$ (eV nm)	-0.0112	-0.00416	-0.0377
$c_{18}$ (eV nm)	0.0055	-0.00109	0.0202
$c_{19}$ (eV nm)	0.801	-0.568	-0.616
$c_{20}$ (eV nm)	0.214	-0.116	-0.298
$c_{21}$ (eV nm)	-0.00918	-0.00423	-0.0294
$c_{22}$ (eV nm <sup>2</sup> )	0.0203	0.0266	0.0282
$c_{23}$ (eV nm <sup>2</sup> )	0.0182	0.00155	-0.0109
$c_{24}$ (eV nm <sup>2</sup> )	0.00486	0.000225	-0.00585
$c_{25}$ (eV nm <sup>2</sup> )	-2.32e-05	8.08e-05	-0.000406
$c_{26}$ (eV nm <sup>2</sup> )	0.273	0.128	0.264
$c_{27}$ (eV nm <sup>2</sup> )	-0.0267	-0.0151	-0.0262
$c_{28}$ (eV nm <sup>2</sup> )	0.00735	0.00235	0.00881
$c_{29}$ (eV nm <sup>2</sup> )	-0.00672	0.00214	-0.00733
$c_{30}$ (eV nm <sup>2</sup> )	-0.0558	-0.0259	-0.0411
$c_{31}$ (eV nm <sup>2</sup> )	0.0285	-0.0109	0.0178
$c_{32}$ (eV nm <sup>2</sup> )	-0.0581	-0.0255	-0.0433
$c_{33}$ (eV nm <sup>2</sup> )	-0.000342	0.00025	0.000387
$c_{34}$ (eV nm <sup>2</sup> )	0.00537	-0.00331	-0.00541
$c_{35}$ (eV nm <sup>2</sup> )	0.0223	-0.0176	-0.017
$c_{36}$ (eV nm <sup>2</sup> )	0.0241	0.0197	-0.0248
$c_{37}$ (eV nm <sup>2</sup> )	0.00671	0.000335	-0.00687
$c_{38}$ (eV nm <sup>2</sup> )	0.0214	0.00371	-0.00757
$c_{39}$ (eV nm <sup>2</sup> )	-0.0229	0.0034	0.0112
$c_{40}$ (eV nm <sup>2</sup> )	0.00903	-0.000739	0.00432
$c_{41}$ (eV nm <sup>2</sup> )	-0.00964	-0.000377	-0.0054
$c_{42}$ (eV nm <sup>2</sup> )	0.00366	-0.000194	0.00471
$c_{43}$ (eV nm <sup>2</sup> )	-7.74e-05	4.97e-06	0.000177
$c_{44}$ (eV nm <sup>2</sup> )	0.0266	0.0241	0.0318
$c_{45}$ (eV nm <sup>2</sup> )	-0.0156	-0.00776	0.00148
$c_{46}$ (eV nm <sup>2</sup> )	-0.00304	-0.00173	-0.0025
$c_{47}$ (eV nm <sup>2</sup> )	0.0326	0.0175	0.031
$c_{48}$ (eV nm <sup>2</sup> )	-0.0661	-0.0482	-0.0636
$c_{49}$ (eV nm <sup>2</sup> )	-0.0107	-0.00713	-0.0205
$c_{50}$ (eV nm <sup>2</sup> )	-0.0334	-0.0158	-0.0379
$c_{51}$ (eV nm <sup>2</sup> )	-0.0294	-0.0139	-0.0242

Table VIII. Table of parameters for the rock-salt materials, where the coefficients  $c_n$  refer to the terms of  $H_{\text{RS}}$  in the equation listed in Table XI.

Rock-salt	PbSe	SnTe
$c_0$ (eV)	0.235	0.125
$c_1$ (eV)	0.284	0.000141
$c_2$ (eV nm)	0.168	0.193
$c_3$ (eV nm)	-0.122	-0.111
$c_4$ (eV nm <sup>2</sup> )	-0.134	-0.713
$c_5$ (eV nm <sup>2</sup> )	0.223	0.214
$c_6$ (eV nm <sup>2</sup> )	0.119	0.637
$c_7$ (eV nm <sup>2</sup> )	-0.151	-0.158

Table IX. Effective Hamiltonian for zincblende crystals considering the  $8 \times 8$  extended Kane model.

$$H_{ZB} = \begin{bmatrix}
c_0 + c_7 k^2 & 0 & i \left( c_{15} k_- k_z - \frac{\sqrt{3} c_{15} k_+}{2} \right) & i \left( c_{15} k_- k_z - \frac{\sqrt{3} c_{15} k_+}{2} \right) & \frac{ic_{12} \cdot (2k_z^2 - k_{\parallel}^2)}{2} \\
0 & c_0 + c_7 k^2 & \frac{ic_{12}(-2k_z^2 + k_{\parallel}^2)}{2} & \frac{ic_{12}(-2k_z^2 + k_{\parallel}^2)}{2} & i \left( c_{15} k_+ k_z + \frac{\sqrt{3} c_{15} k_-}{2} \right) \\
i \left( -c_{15} k_+ k_z + \frac{\sqrt{3} c_{15} k_-}{2} \right) & \frac{ic_{12}(-2k_z^2 + k_{\parallel}^2)}{2} & c_1 + \frac{c_8 \cdot (4k_z^2 + k_{\parallel}^2)}{4} + \frac{3c_9 k_{\parallel}^2}{4} & c_1 + \frac{c_8 \cdot (4k_z^2 + k_{\parallel}^2)}{4} + \frac{3c_9 k_{\parallel}^2}{4} & -\frac{\sqrt{3} c_3 k_-}{2} \\
i \left( -\frac{\sqrt{3} c_{15} k_- k_z - c_5 k_+}{3} \right) & i \left( -c_{15} k_- k_z - \frac{\sqrt{3} c_{15} k_+}{2} \right) & -\frac{\sqrt{3} \hat{K} c_{12}}{2} - \frac{2\sqrt{3} c_{15} k_x k_y - c_5 k_+}{3} - i c_5 k_z & \frac{\sqrt{3} \hat{K} c_8}{4} - \frac{\sqrt{3} \hat{K} c_9}{4} + i c_{13} k_x k_y + c_3 k_z & c_1 + \frac{c_8 \cdot (4k_z^2 + k_{\parallel}^2)}{4} + \frac{3c_9 k_{\parallel}^2}{4} \\
\frac{\sqrt{3} i \hat{K} c_{12}}{2} - \frac{2\sqrt{3} c_{15} k_x k_y - c_5 k_+}{3} - i c_5 k_z & i \left( -\frac{\sqrt{3} c_{15} k_+ k_z + c_5 k_-}{3} + \frac{c_5 k_-}{2} \right) & i \left( -\frac{\sqrt{3} c_{15} k_+ k_z + c_5 k_-}{3} + \frac{c_5 k_-}{2} \right) & \frac{\sqrt{3} \hat{K} c_{10}}{2} + 2i c_{14} k_x k_y + c_4 k_z & c_1 + \frac{c_8 \cdot (4k_z^2 + k_{\parallel}^2)}{4} + \frac{3c_9 k_{\parallel}^2}{4} \\
i \left( -c_{16} k_- k_z - c_6 k_+ \right) & c_{16} k_x k_y + i c_6 k_z & i \left( -c_{16} k_+ k_z - c_6 k_- \right) & \frac{\sqrt{3} \hat{K} c_{10}}{2} + 2i c_{14} k_x k_y + c_4 k_z & c_1 + \frac{c_8 \cdot (4k_z^2 + k_{\parallel}^2)}{4} + \frac{3c_9 k_{\parallel}^2}{4} \\
-c_{16} k_x k_y - i c_6 k_z & i \left( c_{16} k_+ k_z - c_6 k_- \right) & i \left( c_{16} k_+ k_z - c_6 k_- \right) & \frac{\sqrt{3} \hat{K} c_{10}}{2} + 2i c_{14} k_x k_y + c_4 k_z & c_1 + \frac{c_8 \cdot (4k_z^2 + k_{\parallel}^2)}{4} + \frac{3c_9 k_{\parallel}^2}{4} \\
i \left( \frac{\sqrt{3} c_{15} k_+ k_z + c_5 k_-}{3} \right) & i \left( \frac{\sqrt{3} c_{15} k_+ k_z + c_5 k_-}{3} \right) & -\frac{\sqrt{3} i \hat{K} c_{12}}{2} - \frac{2\sqrt{3} c_{15} k_x k_y + i c_5 k_z}{3} & -\frac{\sqrt{3} i \hat{K} c_{12}}{2} - \frac{2\sqrt{3} c_{15} k_x k_y + i c_5 k_z}{3} & i \left( c_{16} k_+ k_z + c_6 k_- \right) \\
\frac{\sqrt{3} i \hat{K} c_{12}}{2} - \frac{2\sqrt{3} c_{15} k_x k_y + i c_5 k_z}{3} & -\frac{\sqrt{3} i \hat{K} c_{12}}{2} - \frac{2\sqrt{3} c_{15} k_x k_y + i c_5 k_z}{3} & i \left( \frac{\sqrt{3} c_{15} k_- k_z - c_5 k_+}{3} - \frac{c_5 k_+}{2} \right) & i \left( \frac{\sqrt{3} c_{15} k_- k_z - c_5 k_+}{3} - \frac{c_5 k_+}{2} \right) & i \left( c_{16} k_- k_z + c_6 k_+ \right) \\
\frac{\sqrt{3} \hat{K} c_8}{4} - \frac{\sqrt{3} \hat{K} c_9}{4} - i c_{13} k_x k_y + c_3 k_z & \frac{\sqrt{3} \hat{K} c_8}{4} - \frac{\sqrt{3} \hat{K} c_9}{4} - i c_{13} k_x k_y + c_3 k_z & \frac{\sqrt{3} \hat{K} c_8}{4} - \frac{\sqrt{3} \hat{K} c_9}{4} - i c_{13} k_x k_y + c_3 k_z & \frac{\sqrt{3} \hat{K} c_8}{4} - \frac{\sqrt{3} \hat{K} c_9}{4} - i c_{13} k_x k_y + c_3 k_z & i \left( -c_{16} k_x k_y + i c_6 k_z \right) \\
c_1 + \frac{c_8 \cdot k_{\parallel}^2}{4} + \frac{c_9 \cdot (4k_z^2 + k_{\parallel}^2)}{4} & c_1 + \frac{c_8 \cdot k_{\parallel}^2}{4} + \frac{c_9 \cdot (4k_z^2 + k_{\parallel}^2)}{4} & c_1 + \frac{c_8 \cdot k_{\parallel}^2}{4} + \frac{c_9 \cdot (4k_z^2 + k_{\parallel}^2)}{4} & c_1 + \frac{c_8 \cdot k_{\parallel}^2}{4} + \frac{c_9 \cdot (4k_z^2 + k_{\parallel}^2)}{4} & i \left( -c_{16} k_x k_y + i c_6 k_z \right) \\
\frac{\sqrt{3} c_3 k_+}{2} & \frac{\sqrt{3} c_3 k_+}{2} & \frac{\sqrt{3} c_3 k_+}{2} & \frac{\sqrt{3} c_3 k_+}{2} & i \left( c_{16} k_+ k_z + c_6 k_- \right) \\
\frac{c_{10} \cdot (2k_z^2 - k_{\parallel}^2)}{2} & \frac{c_{10} \cdot (2k_z^2 - k_{\parallel}^2)}{2} & \frac{c_{10} \cdot (2k_z^2 - k_{\parallel}^2)}{2} & \frac{c_{10} \cdot (2k_z^2 - k_{\parallel}^2)}{2} & i \left( -c_{16} k_x k_y + i c_6 k_z \right) \\
\sqrt{3} \left( -c_{14} k_- k_z + \frac{c_4 k_+}{2} \right) & \sqrt{3} \left( -c_{14} k_- k_z + \frac{c_4 k_+}{2} \right) & \sqrt{3} \left( -c_{14} k_- k_z + \frac{c_4 k_+}{2} \right) & \sqrt{3} \left( -c_{14} k_- k_z + \frac{c_4 k_+}{2} \right) & i \left( -c_{16} k_x k_y + i c_6 k_z \right) \\
\frac{c_{11} k^2 + c_2}{2} & \frac{c_{11} k^2 + c_2}{2} & \frac{c_{11} k^2 + c_2}{2} & \frac{c_{11} k^2 + c_2}{2} & i \left( -c_{16} k_x k_y + i c_6 k_z \right)
\end{bmatrix}$$

Table X. Effective Hamiltonian for wurtzite crystals considering the  $10 \times 10$  model with two conduction bands.

$$H_{WZ} = \begin{bmatrix} c_0 + c_{22}k_{\parallel}^2 + c_{44}k_z^2 & ic_9k_- & 0 & c_{33}(ik_x^2 - 2k_xk_y - ik_y^2) & c_1 + ic_{19}k_z + c_{23}k_{\parallel}^2 + c_{45}k_z^2 \\ -ic_9k_+ & c_0 + c_{22}k_{\parallel}^2 + c_{44}k_z^2 & c_{33}(ik_x^2 + 2k_xk_y - ik_y^2) & 0 & -k_+(ic_{10} + c_{37}k_z) \\ c_{33}(-ik_x^2 - 2k_xk_y + ik_y^2) & c_{33}(-ik_x^2 + 2k_xk_y + ik_y^2) & c_{26}k_{\parallel}^2 + c_3 + c_{47}k_z^2 & ic_{13}k_- & 0 \\ c_1 - ic_{19}k_z + c_{23}k_{\parallel}^2 + c_{45}k_z^2 & k_-(ic_{10} - c_{37}k_z) & 0 & c_{26}k_{\parallel}^2 + c_3 + c_{47}k_z^2 & c_{34}(ik_x^2 + 2k_xk_y - ik_y^2) \\ k_+( -ic_{11} + c_{38}k_z) & c_1 - ic_{19}k_z + c_{23}k_{\parallel}^2 + c_{45}k_z^2 & c_{34}(-ik_x^2 - 2k_xk_y + ik_y^2) & c_{34}(-ik_x^2 + 2k_xk_y + ik_y^2) & c_{27}k_{\parallel}^2 + c_4 + c_{48}k_z^2 \\ k_+(-ic_{20}k_z + c_{24}k_{\parallel}^2 - c_{46}k_z^2) & -c_2 + ic_{20}k_z - c_{24}k_{\parallel}^2 - c_{46}k_z^2 & c_{35}(-ik_x^2 - 2k_xk_y + ik_y^2) & 0 & -ic_{14}k_+ \\ c_2 - ic_{20}k_z + c_{24}k_{\parallel}^2 + c_{46}k_z^2 & k_-( -ic_{11} + c_{38}k_z) & 0 & c_{35}(ik_x^2 - 2k_xk_y - ik_y^2) & k_+(-ic_{15} + c_{40}k_z) \\ k_-( -ic_{12} + c_{39}k_z) & c_{25}(-\hat{K} + 2ik_xk_y) & c_{36}(-ik_x^2 + 2k_xk_y + ik_y^2) & k_+(-ic_{43}k_z + c_8) & -ic_{21}k_z + c_{28}k_{\parallel}^2 + c_{49}k_z^2 + c_5 \\ c_{25}(\hat{K} + 2ik_xk_y) & k_+(-ic_{12} + c_{39}k_z) & k_-( -ic_{12} + c_{39}k_z) & c_{36}(ik_x^2 + 2k_xk_y - ik_y^2) & k_-( -ic_{16} + c_{41}k_z) \\ & k_-(ic_{10} + c_{37}k_z) & k_-(ic_{11} + c_{38}k_z) & c_2 + ic_{20}k_z + c_{24}k_{\parallel}^2 + c_{46}k_z^2 & c_{29}(\hat{K} + 2ik_xk_y) \\ & c_1 + ic_{19}k_z + c_{23}k_{\parallel}^2 + c_{45}k_z^2 & -c_2 - ic_{20}k_z - c_{24}k_{\parallel}^2 - c_{46}k_z^2 & k_+(ic_{12} + c_{39}k_z) & c_{25}(\hat{K} - 2ik_xk_y) \\ & c_{34}(ik_x^2 - 2k_xk_y - ik_y^2) & c_{35}(ik_x^2 - 2k_xk_y - ik_y^2) & -c_{25}(\hat{K} + 2ik_xk_y) & k_-(ic_{12} + c_{39}k_z) \\ & 0 & 0 & c_{36}(ik_x^2 + 2k_xk_y + ik_y^2) & k_+(ic_{43}k_z + c_8) \\ & ic_{14}k_- & 0 & ic_{21}k_z + c_{28}k_{\parallel}^2 + c_{49}k_z^2 + c_5 & c_{36}(-ik_x^2 + 2k_xk_y + ik_y^2) \\ & c_{27}k_{\parallel}^2 + c_4 + c_{48}k_z^2 & -ic_{21}k_z - c_{28}k_{\parallel}^2 - c_{49}k_z^2 - c_5 & -c_{29}(\hat{K} + 2ik_xk_y) & c_{29}(\hat{K} - 2ik_xk_y) \\ & ic_{21}k_z - c_{28}k_{\parallel}^2 - c_{49}k_z^2 - c_5 & c_{30}k_{\parallel}^2 + c_{50}k_z^2 + c_6 & k_+(ic_{15} + c_{40}k_z) & k_-(ic_{16} + c_{41}k_z) \\ & k_-( -ic_{15} + c_{40}k_z) & -ic_{17}k_- & ic_{17}k_+ & k_-(ic_{18} + c_{42}k_z) \\ & c_{29}(-\hat{K} + 2ik_xk_y) & c_{31}(\hat{K} - 2ik_xk_y) & -k_+(ic_{18} + c_{42}k_z) & c_{31}(\hat{K} - 2ik_xk_y) \\ & k_+(-ic_{16} + c_{41}k_z) & k_+(-ic_{18} + c_{42}k_z) & c_{32}k_{\parallel}^2 + c_{51}k_z^2 + c_7 & 0 \\ & & & 0 & c_{32}k_{\parallel}^2 + c_{51}k_z^2 + c_7 \\ & & & & 0 \end{bmatrix}$$



Table XI. Effective Hamiltonian for rock-salt crystals considering the  $4 \times 4$  model composed by the  $L_6^\pm$  irreps of  $D_{3D}$ .

---


$$H_{\text{RS}} = \begin{bmatrix} c_0 + c_4 k^2 + c_6 (k_x k_y + k_x k_z + k_y k_z) & 0 & c_0 + c_4 k^2 + c_6 (k_x k_y + k_x k_z + k_y k_z) & 0 \\ 0 & c_0 + c_4 k^2 + c_6 (k_x k_y + k_x k_z + k_y k_z) & c_2 (-ik_- + k_z (1+i)) & c_2 (-ik_- + k_z (1+i)) \\ -c_2 (k_x - k_y) - ic_3 (k_x + k_y + k_z) & c_2 (-ik_- + k_z (1+i)) & c_2 (k_x - k_y) - ic_3 (k_x + k_y + k_z) & c_2 (k_x - k_y) + ic_3 (k_x + k_y + k_z) \\ c_2 (ik_+ + k_z (1-i)) & c_2 (k_x - k_y) - ic_3 (k_x + k_y + k_z) & -c_2 (k_x - k_y) + ic_3 (k_x + k_y + k_z) & c_2 (k_x - k_y) + ic_3 (k_x + k_y + k_z) \\ & & c_2 (ik_+ + k_z (1-i)) & c_2 (k_x - k_y) + ic_3 (k_x + k_y + k_z) \\ & & c_1 + c_5 k^2 + c_7 (k_x k_y + k_x k_z + k_y k_z) & 0 \\ & & 0 & c_1 + c_5 k^2 + c_7 (k_x k_y + k_x k_z + k_y k_z) \end{bmatrix}$$


---